

The Deep Chandra Survey of the Groth Strip - II. optical identification of the X-ray sources

A. Georgakakis¹*, K. Nandra¹, E. S. Laird¹, S. Gwyn², C. C. Steidel³, V. L. Sarajedini⁴, P. Barmby⁵, S. M. Faber⁶, A. L. Coil⁷, M. C. Cooper⁸, M. Davis^{8,9}, J. A. Newman¹⁰

¹Astrophysics Group, Blackett Laboratory, Imperial College, Prince Consort Rd, London SW7 2BZ, UK

²Department of Physics and Astronomy, University of Victoria, P.O. Box 3055, Victoria, BC V8W 3P6, Canada.

³California Institute of Technology, Pasadena, CA 91125, USA

⁴University of Florida, Department of Astronomy, Gainesville, FL 32611, USA

⁵Harvard-Smithsonian Center for Astrophysics, 60 Garden Street, Mail Stop 65, Cambridge, MA 02138, USA

⁶UCO/Lick Observatory and Department of Astronomy and Astrophysics, University of California, Santa Cruz, CA 95064, USA

⁷Steward Observatory, University of Arizona, 933 N. Cherry Ave., Tucson, AZ 85721-0065, USA

⁸Department of Astronomy, University of California, Berkeley, CA 94720

⁹Department of Physics, University of California, Berkeley, CA 94720

¹⁰Hubble Fellow; Institute for Nuclear and Particle Astrophysics, Lawrence Berkeley National Laboratory, Berkeley, CA 94720

21 September 2018

ABSTRACT

In this paper we discuss the optical and X-ray spectral properties of the sources detected in a single 200ks *Chandra* pointing in the Groth-Westphal Strip region. A wealth of optical photometric and spectroscopic data are available in this field providing optical identifications and redshift determinations for the X-ray population. The optical photometry and spectroscopy used here are primarily from the DEEP2 survey with additional redshifts obtained from the literature. These are complemented with the deeper ($r \approx 26$ mag) multi-waveband data (*ugriz*) from the Canada France Hawaii Legacy Survey to estimate photometric redshifts and to optically identify sources fainter than the DEEP2 magnitude limit ($R_{AB} \approx 24.5$ mag). We focus our study on the 2–10 keV selected sample comprising 97 sources to the limit $\approx 8 \times 10^{-16}$ erg s^{−1} cm^{−2}, this being the most complete in terms of optical identification rate (86%) and redshift determination fraction (63%; both spectroscopic and photometric). We first construct the redshift distribution of the sample which shows a peak at $z \approx 1$. This is in broad agreement with models where less luminous AGNs evolve out to $z \approx 1$ with powerful QSOs peaking at higher redshift, $z \approx 2$. Evolution similar to that of broad-line QSOs applied to the entire AGN population (both type-I and II) does not fit the data. We also explore the *observed* N_H distribution of the sample and estimate a fraction of obscured AGN ($N_H > 10^{22}$ cm^{−2}) of 48 ± 9 per cent. This is found to be consistent with both a luminosity dependent *intrinsic* N_H distribution, where less luminous systems comprise a higher fraction of type-II AGNs and models with a fixed ratio 2:1 between type-I and II AGNs. We further compare our results with those obtained in deeper and shallower surveys. We argue that a luminosity dependent parametrisation of the *intrinsic* N_H distribution is required to account for the fraction of obscured AGN observed in different samples over a wide range of fluxes.

Key words: Surveys – galaxies: active – X-rays: galaxies – X-rays: diffuse background – cosmology: observations

1 INTRODUCTION

In the last few years the study of the diffuse X-ray background (XRB) has witnessed significant observational progress allowing detailed comparison with model predictions. The ultra-deep *Chandra*

surveys in particular, have demonstrated that most of the XRB, at both soft and hard energies, is resolved into discrete point sources (Brandt et al. 2001; Giacconi et al. 2002; Alexander et al. 2003), the vast majority of which are without doubt AGNs. To the first approximation, this finding has been a huge success for models that reproduce the spectral properties of the XRB under the zero order assumption that it originates in a combination of obscured and unob-

* Marie Curie fellow

scured AGN (Comastri et al. 1995; Gilli, Salvati & Hasinger 2001). Under more careful examination however, a number of inconsistencies emerge. Firstly, luminous ($L_X > 10^{44} \text{ erg s}^{-1}$) heavily obscured type-II QSOs at $z \approx 1.5 - 2$, predicted in large numbers by the models, are scarce in the surveys above. Secondly, the redshift peak of the X-ray population lies below $z = 1$ in stark contrast with the model expectation of $z \approx 1.5 - 2$.

Although these inconsistencies suggest that some revision of the models is almost certainly required (Hasinger 2003), observational biases may complicate any interpretation. For example, about ≈ 25 per cent of the sources in the *Chandra* Deep Fields (CDF) are optically faint, $R > 24$ mag, rendering optical spectroscopy difficult or even impossible with current technology (Rosati et al. 2002; Barger et al. 2003). Any information about the nature of these sources is therefore limited and they are proposed as best candidates for heavily obscured AGN (Alexander et al. 2001; Treister et al. 2004), likely to comprise a fraction the elusive population of high- z type-II QSOs. Moreover, the small field-of-view of the CDFs (0.07 deg^2 each) makes them sensitive to cosmic variance further complicating interpretation of the derived redshift distribution.

Wide-area shallower ($\approx 10^{-14} \text{ erg s}^{-1} \text{ cm}^{-2}$) surveys are less affected by the observational biases above (e.g. Baldi et al. 2002; Kim et al. 2004; Georgantopoulos et al. 2004). These samples although of key importance, comprise a large fraction of unobscured AGNs that are not representative of the sources responsible for the spectral shape of the XRB ($\Gamma = 1.4$; e.g. Gruber et al. 1999).

The evidence above suggests that deep surveys with relatively wide field-of-view are essential to improve our understanding of the XRB. Observational programs in this direction are already well underway such as the *XMM-Newton* Cosmic Evolution Survey [COSMOS; 2 deg^2 , $f_X(0.5 - 2 \text{ keV}) \approx 5 \times 10^{-16} \text{ erg s}^{-1} \text{ cm}^{-2}$] and the Extended *Chandra* Deep Field South [E-CDF-S; Lehmer et al. 2005; Virani, Treister & Urry 2006; 0.3 deg^2 , $f_X(0.5 - 2 \text{ keV}) \approx 1.1 \times 10^{-16} \text{ erg s}^{-1} \text{ cm}^{-2}$]. In this paper we present results on a single 200 ks *Chandra* pointing, which is part of an on-going X-ray survey in the Extended Groth Strip region, which will eventually cover a total area of about 0.5 deg^2 to the depth above (200 ks per pointing). This sample, when completed, will be intermediate in terms of area coverage and depth to the CDFs and shallower wide-area surveys, minimising any observational biases affecting the ultra-deep fields and comprising a large fraction of obscured AGNs responsible of the XRB properties (Nandra et al. 2005). Moreover, the Extended Groth Strip is targeted by the largest space and ground-based facilities for multiwavelength observations: (i) the DEEP and DEEP2 surveys provide optical spectroscopy to the limit $R_{AB} \approx 24$ mag, (ii) multiwaveband optical photometry to fainter magnitudes is underway as part of the Canada France Hawaii Telescope Legacy Survey, (iii) deep imaging and spectroscopy, independent from the programs above, has been performed by Steidel et al. (2003) in search for Lyman break galaxies, (iv) comprehensive imaging with HST/ACS has recently been completed, (v) *Spitzer* mid-IR data are available, (vi) radio observations to sub-mJy levels have been obtained by Fomalont et al. (1991) with new much wider VLA observations recently completed, (vii) SCUBA has observed part of this field to the deep limits of the Canada-UK Deep Submillimetre survey (Webb et al. 2003). A combination of the X-ray observations with the multiwavelength datasets above promises a breakthrough in the study of the evolution and large scale structure of AGNs as well as the connection between AGN activity and host galaxy formation.

This paper presents the optical and X-ray spectral properties of the sources detected in the first 200 ks *Chandra* pointing observed as part of the Extended Groth Strip X-ray survey. This observation encompasses the original Groth-Westphal Strip region (Groth et al. 1994). In addition to studying the properties of the X-ray sources in the context of XRB models, our purpose is to demonstrate the power of the full 0.5 deg^2 Extended Groth Strip *Chandra* survey, when completed, for XRB studies. Throughout this paper we adopt $Ho = 70 \text{ km s}^{-1} \text{ Mpc}^{-1}$, $\Omega_M = 0.3$ and $\Omega_\Lambda = 0.7$.

2 DATA

2.1 X-ray observations

The X-ray data used in this paper are from the A03 *Chandra* observations of the original Groth Westphal Strip (GWS), which is part of the Extended Groth Strip (EGS) region. The total exposure time is about 190 ks split into 3 separate integrations obtained at different epochs. All 3 observations were obtained with the ACIS-I instrument ($17' \times 17'$) with a similar roll-angle at the aimpoint, $\alpha = 14:17:43.6$, $\delta = 52:28:41.2$. A detailed description of the data reduction, source detection and flux estimation has been presented by Nandra et al. (2005).

Briefly, standard reduction methods were applied using the CIAO version 3.0.1 data analysis software. After merging the individual observations into a single event file, we constructed images in 4 energy bands 0.5-7.0 keV (full), 0.5-2.0 keV (soft), 2.0-7.0 keV (hard) and 4.0-7.0 keV (ultra-hard). Source detection was performed using a simple but efficient method which is based on pre-selection of candidate sources using the WAVDETECT task of CIAO followed by aperture count extraction using the 90 per cent Point Spread Function (PSF) radius and a local background determination to estimate the source significance. The final catalogue used in this paper comprises a total of 158 sources over a total surveyed area of 0.082 deg^2 to a Poisson detection probability threshold $< 4 \times 10^{-6}$. Of these sources a total of 155, 121, 97, and 44 are detected in the full, soft, hard and ultra-hard bands respectively. Fluxes are estimated by integrating the net counts within an aperture corresponding to the 70 per cent encircled energy radius at the position of the source. The counts in the full, soft, hard and ultra-hard bands are converted into fluxes in standard bands, 0.5-10, 0.5-2, 2-10 and 5-10 keV respectively. The limiting flux in each of these bands is estimated 3.5×10^{-15} , 1.1×10^{-16} , 8.2×10^{-16} and $1.4 \times 10^{-15} \text{ erg s}^{-1} \text{ cm}^{-2}$ respectively.

2.2 Optical photometry

The main photometric catalogue used in this paper for the optical identification of the X-ray sources is the DEEP2 survey of the EGS that also overlaps with the original GWS field.

The DEEP2 survey photometric data were obtained at the Canada-France-Hawaii Telescope (CFHT) using the $12k \times 8k$ pixel CCD mosaic camera providing a $0.70 \times 0.47 \text{ deg}^2$ field of view per pointing. The observations were performed in the B , R and I filters. The data reduction, source detection, photometric and astrometric calibration as well as the star-galaxy separation are described in Coil et al. (2004). The pointing that overlaps with the *Chandra* X-ray data used here is nearly complete to $R_{AB} \approx 24.50$ mag ($B_{AB} \approx 24.75$, $I_{AB} \approx 23.5$ mag). This is shallower than the nominal limit of the full DEEP2 EGS survey ($R_{AB} \approx 24.75$ mag) because of poorer seeing conditions (about

0.95 arcsec) at the time of the observations (Coil et al. 2004). The astrometric accuracy of the photometric catalogue is estimated to be 0.5 arcsec and is limited by systematic errors of the USNO-A catalogue used to determine the astrometric solution.

The GWS also overlaps with the ongoing deep synoptic Canada-France-Hawaii Telescope Legacy Survey (CFHTLS). This project uses the wide field imager MegaPrime equipped with the MegaCam CCD array providing a 1×1 deg 2 field of view. In this paper we use the first data obtained as part of the deep synoptic survey in the *ugriz* filters. The exposure times in each waveband range from 1–13 hours (depending on the filter) corresponding to about 2–9 per cent of the target integration at the completion of the project. The data reduction, source detection, photometric and astrometric calibration will be presented in a future paper. In brief the Elixir package was used for the reduction as well as the initial photometric and astrometric calibration, which were then refined using our own routines. The final astrometric uncertainty is estimated to be about 0.3 arcsec. The photometric accuracy is found to be better than 0.05 mag in all filters while the completeness limit in the AB system is $r \approx 26$ mag ($u \approx 25.5$, $g \approx 26.0$, $i \approx 25.5$, $z \approx 25.0$ mag). Although the CFHTLS deep synoptic dataset reaches fainter limits than the DEEP2, we prefer to use the latter at present as the basic photometric catalogue because of its homogeneity and the well documented observational properties of this survey (e.g. Coil et al. 2004; Faber et al. 2005; Willmer et al. 2005). We nevertheless use the multi-waveband photometry of the CFHTLS primarily to estimate photometric redshifts but also to search for X-ray source optical counterparts that are fainter than the DEEP2 limit.

Finally, the GWS has been targeted for deep optical imaging as part of a larger program searching for Lyman Break galaxies (Steidel et al. 2003). The observations were performed at the Kitt Peak 4m Mayall telescope using the Prime Focus CCD camera (14.2×14.2 deg 2 field of view) in the *Un*, *G* and *R* filters. Because of the smaller field-of-view of these observations the outer edges of X-ray pointing do not overlap with the optical image. A detailed description is presented by Steidel et al. (2003). The astrometry is accurate to about 0.4 arcsec and the photometric internal scatter is estimated to be better than 0.03 mag in all filters. These observations reach a limiting magnitude $R_{AB} \approx 26$ mag, similar to the CFHTLS. They are used here primarily to estimate photometric redshifts using the Lyman break selection criteria. As discussed by Steidel et al. (2003), these methods are very efficient in identifying galaxies in narrow redshift slices in the range $1.5 \lesssim z \lesssim 3$.

We note that the *R*-band filters used in the above three datasets are similar and therefore, there is good agreement in the estimated *R*-band magnitudes of the same object among the different surveys.

2.3 Optical spectroscopy

The main source of optical spectroscopy in this study is the DEEP2 redshift survey. This is an ongoing project that uses the DEIMOS spectrograph on the 10 m Keck II telescope aiming to obtain redshifts for about 40 000 galaxies in the range $0.7 \lesssim z \lesssim 1.5$ to a limiting magnitude $R_{AB} = 24.1$ mag. The spectra are obtained with a high resolution grating (1200 l/mm, $R \approx 5000$) and span the wavelength range 6500–9100 Å. This spectral window allows the identification of the O II emission line in the redshift interval $0.7 \lesssim z \lesssim 1.4$. Outside this range the ability to measure redshifts and hence, the completeness of the DEEP2, drops significantly. The data reduction was performed using an IDL based pipeline devel-

oped at UC-Berkeley (Cooper et al. 2006) and adapted from reduction programs created for the SDSS.

The GWS has also been targeted by a number of spectroscopic programs (Lilly 1995; Brinchmann et al. 1998; Hopkins et al. 2000; Voght et al. 2005) that have been compiled into a single database by Weiner et al. (2005¹). The entire EGS overlaps with the Sloan Digital Sky Survey (SDSS) and therefore spectra for relatively bright galaxies and QSOs are also available (York et al. 2000).

In addition to the above surveys Steidel et al. (2003, 2004) performed follow-up multi-slit spectroscopy of the GWS Lyman Break galaxies as well as some X-ray sources using the LRIS-B on the Keck telescopes. The observations used a 300 line/mm grating blazed at 5000 Å leading to a dispersion of 2.47 Å/pixel, a wavelength range that included at least the 4000–7000 Å regime and a nominal spectral resolution of about 12.5 Å. The total integration time varied between 1.5–3 h (depending on the observing conditions), split into 1800 s sub-exposures followed by a dither of the telescope in the slit direction. The data were reduced using a custom package based on IRAF scripts. A total of 10 sources in our sample have redshift measurements from these observations.

3 OPTICAL IDENTIFICATION

The main catalogue used to optically identify the GWS X-ray sources is the DEEP2 survey. We first search for systematic offsets between the astrometric solutions of the X-ray and optical catalogues. A matching radius of 2 arcsec is adopted to include only secure optical identifications. We also consider X-ray sources with off-axis angles < 6 arcmin (total of 86) where the *Chandra* PSF is superior with a 90 per cent encircled energy radius of $\lesssim 4$ arcsec. A total of 50 X-ray sources have optical identifications brighter than $R_{AB} < 24.5$ mag. We estimate small systematic offsets of $\delta\text{RA} = -0.23$ and $\delta\text{DEC} = 0.37$ arcsec between the X-ray and optical source positions. These were then used to align the X-ray source catalogue to the DEEP2 astrometric solution.

Next we explore the positional accuracy of the X-ray centroid as a function of off-axis angle, θ . We match the X-ray and optical catalogues using an ample 5 arcsec search radius to account for the degradation of the PSF at large off-axis angles. Figure 1 plots the positional offset in RA and DEC between the X-ray and optical source positions against θ . Reassuringly, the mean X-ray–optical offset is close to zero at all off-axis angles but the 1σ rms increases from about 0.5 arcsec at $\theta \lesssim 6$ arcmin to ≈ 1 arcsec at larger off-axis angles. We account for the degradation of the X-ray positional accuracy by varying the matching radius as a function of off-axis angle. For $\theta \leq 6$ arcmin we use a radius of 1.5 arcsec, corresponding to the 3σ rms scatter around the mean. For $\theta > 6$ arcmin the matching radius increases to 3 arcsec, the 3σ rms positional uncertainty at these off-axis angles.

The surface density of optical sources to the limit $R_{AB} = 24.5$ mag is large enough that a substantial fraction of chance associations is expected within the above radii. We account for this effect by estimating the Poissonian probability, P , that a given optical counterpart is spurious alignment following the method of Downes et al. (1986). Given the surface density of objects brighter than m , $\Sigma(< m)$, the expected number of candidates within r is $\mu = \pi r^2 \Sigma(< m)$. Assuming that source positions are Poissonian, the probability of at least one object brighter than m within radius

¹ <http://saci.ucolick.org/verdi/public/index.html>

r is $P = 1 - \exp(-\mu)$. In practice one has to apply a cutoff in P to limit the optical identifications to those candidates that are least likely to be spurious alignments.

The probability P however, is estimated under the assumption that the source positions are uniformly distributed within the surveyed area. For the real clustered distribution of optical sources we assess the fraction of spurious optical identifications for different probability cutoffs using mock X-ray catalogues constructed by randomising the positions of the X-ray sources within the area covered by the *Chandra* observations. The optical identification method is performed on the mock catalogues using the same criteria (e.g. matching radius) as for the real sources. This procedure is repeated 500 times. When constructing random X-ray catalogues we maintain the spatial distribution of the sources due to both vignetting and real clustering. This is accomplished by applying offsets in the range 30–60 arcsec to the X-ray source positions around their original centroid.

Figure 2 plots the cumulative distribution of optical identifications for the full-band X-ray selected sample (using the matching radius scheme described above) as a function of probability cutoff. Also shown in Figure 2 is the expected number of spurious counterparts estimated as described above. This figure shows that the number of optically identified sources reaches a plateau at $P \approx 1.5$ per cent while the spurious identification rate further increases with P . Based on Figure 2 we adopt a cutoff probability $P < 2$ per cent for optical identification in the case of off-axis angles < 6 arcmin. Because of the degradation of the positional accuracy at larger off-axis angles we relax the probability cutoff to $P < 4$ for sources with $\theta > 6$ arcmin. This is to minimise the fraction of missed optical identifications because of the poor X-ray positions. For an optical source with $R_{AB} = 24.5$ mag the probabilities $P < 2$ and $P < 4$ per cent correspond to maximum separations between the optical and X-ray centroids of about 1 and 1.5 arcsec respectively. Repeating the simulations above using the off-axis dependent identification scheme we estimate a spurious fraction of about 4.5 per cent. The choice of P is a trade-off between maximum number of optical counterparts and minimum contamination rate. Similar results and false identification rates are obtained for the soft, hard and ultra-hard samples.

For X-ray sources with no optical identification to the DEEP2 magnitude limit or outside the DEEP2 field-of-view we use the CFHTLS to search for fainter optical counterparts applying the same selection criteria described above. Moreover, a number of optically faint X-ray sources lie in the gaps between the CCDs of the MegaCam mosaic. For these sources we use the Steidel et al. (2003) deep optical imaging to search for optical identifications. Considering sources fainter than the DEEP2 magnitude limit increases the spurious fraction rate by about 2 per cent. A total of 29 sources are identified with galaxies from the CFHTLS or the Steidel et al. (2003) survey. Table 1 summarises the identification statistics for different X-ray selected subsamples. Table 2 presents the optical properties of the GWS X-ray sources as well as the source of optical photometry.

4 REDSHIFT ESTIMATION

Spectroscopic redshifts are available for a total of 51 sources. These are classified into 3 groups on the basis of their optical spectroscopic properties (primarily from DEEP1 and DEEP2) following methods described in Sarajedini et al. (2006): broad emission-line galaxies, narrow emission-line sources and systems with absorption

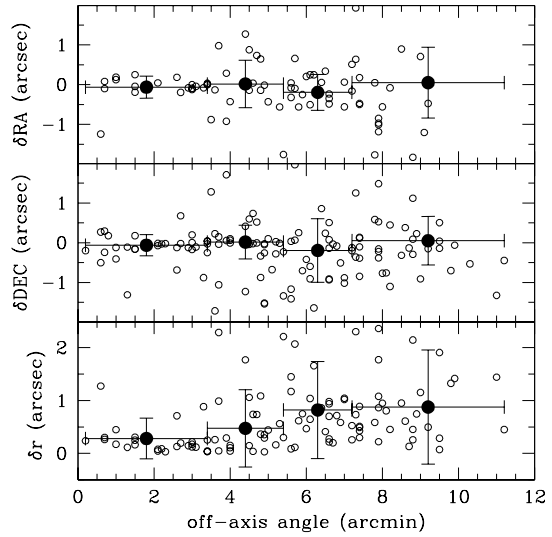


Figure 1. X-ray/optical positional offset in RA (upper panel), DEC (middle panel) and total angular distance (lower panel) against X-ray off-axis angle. The filled points represent the mean offset within different off-axis angle bins. The horizontal errorbar corresponds to the width of each bin while, the vertical errorbar is the 1σ rms. The width of the bins varies so that each of them includes about 25 X-ray/optical pairs.

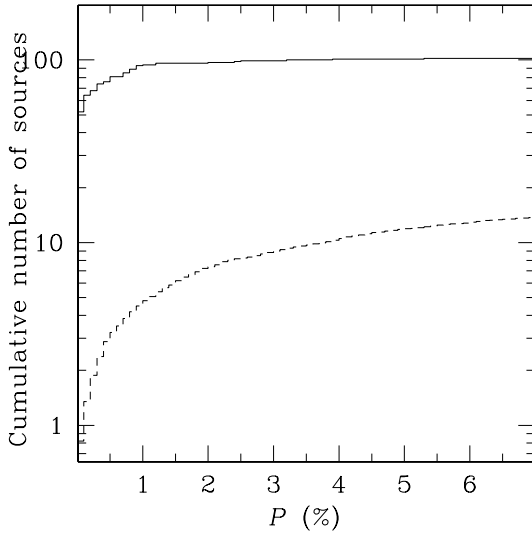


Figure 2. Number of optical identifications as a function of probability cutoff P for the full-band sample. The continuous histogram is for the real X-ray catalogue. The dashed line corresponds to the mean of 500 mock X-ray catalogues as described in the text.

tion lines. For broad emission line AGN we adopt the criterion $\text{FWHM} > 1200 \text{ km s}^{-1}$. We note that the low S/N ratio of some of the spectra and the small spectral window of the DEEP2 observations (6000 – 9500 Å) introduce some uncertainty in the classification scheme above. In addition to the above three groups, a number of sources in the sample cannot be classified because the optical spectra were not available for visual inspection.

For X-ray sources without spectroscopic identification we es-

timate photometric redshifts exploiting the multiwaveband photometry (*ugriz*) of the CFHTLS. Determining photometric redshifts for X-ray sources is challenging because of the significant, if not dominant, AGN component contributing to the optical broadband colours (e.g. Babbedge et al. 2005; Kitsionas et al. 2005). Recent studies however, suggest that many moderate luminosity AGN ($\lesssim 10^{44} \text{ erg s}^{-1}$) as well as obscured X-ray sources have optical continuum emission that is dominated by stellar light thus, allowing galaxy templates to be used for photometric redshifts (Barger et al. 2003; Gandhi et al. 2004; Georgakakis et al. 2004; Georgakakis et al. 2006).

We explore this possibility using the photometric redshift code of Gwyn (2001) based on a standard χ^2 minimisation method. The galaxy templates are based on those of Coleman, Wu & Widman (1980), providing SEDs for 4 main spectral galaxy types (E/S0, Sbc, Scd, Im), extended in the UV and IR wavelength regions using the GISSEL98 code (e.g. Bruzual & Charlot 1993). These are supplemented with the starburst SB2 and SB3 spectra from Kinney et al. (1996). Having only a small number of SEDs can cause aliasing in photometric redshifts. Therefore, a new template set has been created by smoothly interpolating between each of the six original spectra. This results in a total 51 SEDs from ellipticals (spectral classification 0) to extreme starbursts (spectral classification 1).

Figure 3 compares the photometric and spectroscopic redshift estimates for the sources with available spectroscopic observations. With the exception of broad-line QSOs, for which galaxy templates are inappropriate for photometric redshift estimates, there is fair agreement between z_{spec} and z_{phot} with an rms scatter, after excluding broad-line AGN, $\frac{1}{N} \sum \left(\frac{z_{\text{phot}} - z_{\text{spec}}}{1 + z_{\text{spec}}} \right)^2 = 0.08$, where N is the total number of sources. This is further demonstrated in Figure 4 plotting $\delta z = (z_{\text{phot}} - z_{\text{spec}})$ against $B - I$ colour. Sources bluer than $B - I \approx 1.5$ are dominated by broad-line QSOs and show significant scatter in their photometric redshift determination (e.g. Barger et al. 2003; Kitsionas et al. 2005). For systems redder than this limit however, the photometric redshifts are more reliable. To avoid erroneous redshift estimates in the analysis that follows we use photometric redshifts only for sources with $B - I > 1.5$ mag.

In addition to the standard photometric redshift estimation above, we exploit the Lyman Break galaxy selection available for the GWS (Steidel et al. 2003, 2004) to determine the redshift of a small number of X-ray sources. This method has been shown to be very efficient in identifying galaxies in well defined narrow redshift slices within the range $1.5 \lesssim z \lesssim 3$ with a low interloper rate. Here we use the BM, BX, C, D, M and MD Lyman Break galaxy selection criteria fully described in Steidel et al. (2003, 2004), which correspond respectively to redshifts 1.70 ± 0.34 , 2.20 ± 0.34 , 3.09 ± 0.22 , 2.93 ± 0.26 , 3.15 ± 0.24 and 2.79 ± 0.27 . In our sample there are 7 X-ray sources that fulfill one of the above selection criteria: 2 BX, 2 MD, 1 C, 1 D and 1 M.

The optical spectroscopic and photometric redshift information for the GWS sample is presented in Table 2. For the full and hard band samples Figure 5 presents the optical magnitude distribution of sources with spectroscopic, photometric or no redshift information as well as sources without optical identification. The total number of sources in these groups for different X-ray selected samples is also shown in Table 1. The no-redshift class involves sources that are either too faint to estimate photometric redshifts, do not have CFHTLS data (e.g. CCD gaps) or have counterparts with $B - I < 1.5$ mag and therefore unreliable redshift determination.

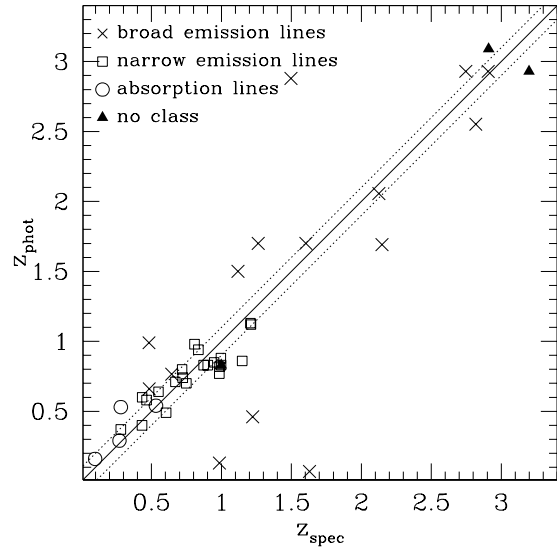


Figure 3. Photometric against spectroscopic redshift estimates for the X-ray sources with available spectroscopic observations. Circles are for sources with absorption-line spectra, squares correspond to systems with narrow emission-line spectra and crosses are broad line AGNs. Triangles are sources with no classification.

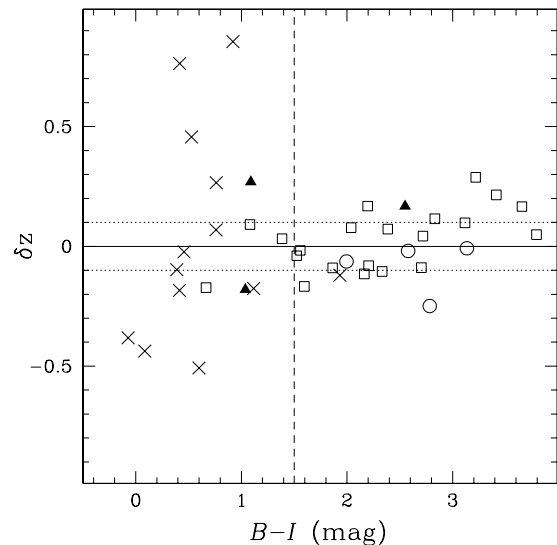


Figure 4. $\delta z = (z_{\text{phot}} - z_{\text{spec}})$ against DEEP2 $B - I$ colour. The symbols are the same as in Figure 3.

5 X-RAY SPECTRA

For the X-ray spectral analysis we use the XSPEC v11.3.1 package. The X-ray counts of each source are extracted using the 95 per cent encircled energy radius (1.5 keV) at the position of the source. The background is estimated using an annulus centered on the source with inner aperture size 1.5 times larger than the 95 per cent encircled energy radius and outer aperture 100 pixel greater. We fit the data adopting a power-law model absorbed by both an intrinsic column density at the redshift of the source and a Galactic column at $z = 0$ fixed to $N_H = 1.3 \times 10^{20} \text{ cm}^{-2}$, appropriate for the EGS (WABS*ZWABS*POW). For the absorption we adopt the Wiscon-

X-ray sub-sample	total number	optical IDs	spectro- z only	photo- z only	optical ID, no- z	no-ID
Total	155	128	51	36	42	27
Soft	121	102	42	27	33	19
Hard	97	83	37	24	22	14
Ultra-hard	44	40	23	10	7	4

Table 1. Optical and spectroscopic identification statistics. The columns are: (1) X-ray sub-sample; (2) total number of X-ray sources; (3) number of optical counterparts; (4) number of spectroscopic identifications; (5) number of sources with photometric redshift determination only (i.e. not spectroscopic z); (6) number of sources with optical counterparts for which photometric redshift estimations was not possible; (7) number of blank fields.

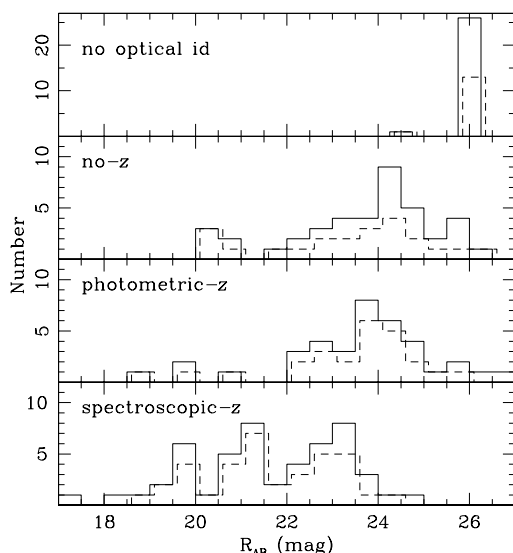


Figure 5. R_{AB} optical magnitude distribution for different subsamples of X-ray sources. The four panels from bottom to top plot respectively histograms for sources with spectroscopic redshifts, photometric redshifts only, without any redshift determination (but with an optical ID) and with no optical identification. Within each panel the continuous line corresponds to the full-band sample and the dashed line (offset to the right by 0.1 mag for clarity) represents the hard sample.

sin cross-sections (Morrison and McCammon 1983). For sources without spectroscopic or photometric redshift estimates we assume $z = 1.5$ to estimate the intrinsic N_H . Adopting a different mean z in the range 1–2 for these systems however, does not significantly modify our results and conclusions.

In the case of sources with small number of net counts ($\lesssim 200$) we use the C-statistic technique (Cash 1979) specifically developed to extract information from low signal-to-noise ratio spectra. The data are grouped to have at least one count per bin. We attempt to constrain the intrinsic N_H by fixing the power-law index to $\Gamma = 1.8$. This value of Γ is selected to be inbetween the mean spectral index of radio loud ($\Gamma = 1.6$; Reeves & Turner 2000; Gambill 2003) and radio quiet AGNs ($\Gamma \approx 1.9$; Nandra & Pounds 1994; Reeves & Turner 2000). Adopting a single fixed Γ for the spectral analysis is an approximation. We caution that our analysis will overestimate the N_H for sources with spectra intrinsically flatter than $\Gamma = 1.8$.

For sources with sufficient number of counts ($\gtrsim 200$) we perform standard χ^2 spectral fitting. The data were grouped to have a minimum of 20 counts per bin to ensure that Gaussian statistics

apply. For the χ^2 analysis we require that the source spectrum has at least 10 spectral bins. The WABS*ZWABS*POW model provides acceptable fits (i.e. reduced $\chi^2 \approx 1$) for all sources. The parameters estimated from the C-statistic and the χ^2 analysis are consistent within the errors.

For both the χ^2 and the C-statistic analysis the fit was performed in the 0.5–8 keV energy range where the sensitivity of the *Chandra* is the highest. The estimated errors correspond to the 90 per cent confidence level. The results of the X-ray spectral analysis are presented in Table 2.

6 THE MODEL

In this section we describe the model we use to interpret the optical and X-ray properties of the GWS X-ray sources in the context of AGN evolution scenarios and different parameterisations for the intrinsic N_H distribution. Modeling of the data requires certain assumptions about the X-ray spectra of AGN, their luminosity function and its evolution with redshift as well as the relative fraction of obscured and unobscured systems.

We model the X-ray spectra of AGN adopting for simplicity an absorbed power-law spectral energy distribution with fixed exponent $\Gamma = 1.8$ and photoelectric absorption cross sections as described by Morrison & McCammon (1983) for solar metallicity.

For the X-ray luminosity function (XLF) of AGNs and its evolution with redshift we use the two different parameterisations presented by Miyaji et al. (2000) and Ueda et al. (2003).

Miyaji et al. (2000) combined deep pencil-beam and shallow wide-area *ROSAT* surveys to estimate the XLF of unobscured AGNs in the rest-frame 0.5–2 keV energy band. We adopt the luminosity dependent density evolution parameterisation of the XLF proposed by Miyaji et al. (their model LDDE1). These authors argue that this model provides a better description of the observations compared to the pure density or luminosity evolution. In this picture AGNs evolve differentially with more luminous systems evolving faster than less luminous ones. Such a trend has also been proposed for the optical luminosity function of QSOs (e.g. Wisotzki 1998).

Ueda et al. (2003) estimated the AGN XLF in the rest-frame 2–10 keV energy range using a combination of hard-band (> 2 keV) surveys conducted with *HEAO-1*, *ASCA* and *Chandra* missions. Here we adopt the luminosity dependent density evolution of the luminosity function, which according to Ueda et al. provides a better fit to the data. In this parameterisation the cutoff redshift, after which the evolution of AGN stops, increases with luminosity. We note that this is different from the Miyaji et al. (2000) luminosity dependent density evolution, where it is the rate of evolution that changes with luminosity but not the cutoff redshift.

For the AGN N_H distribution, $f(N_H)$, we experiment with

different parameterisations. The first model adopted here is the one estimated by Ueda et al. (2003) on the basis of observational data and for column densities in the range $10^{20} < N_H < 10^{24} \text{ cm}^{-2}$. The interesting feature of their functional form is that the fraction of obscured AGNs drops with increasing luminosity. In that sense the Ueda et al. (2003) $f(N_H)$ does not strictly follow the unified model prescription (Antonucci 1993) where the only parameter determining the obscuring column density is the viewing angle to the observer. We also consider a set of models where $f(N_H)$ is a step function with a fixed ratio, \mathcal{R} , between absorbed ($N_H > 10^{22} \text{ cm}^{-2}$) and unabsorbed ($N_H < 10^{22} \text{ cm}^{-2}$) sources. We further assume that obscured and unobscured AGNs are distributed uniformly in the range $10^{20} < N_H < 10^{22}$ and $10^{22} < N_H < 10^{26} \text{ cm}^{-2}$ respectively. For the obscured systems, the above assumption is in fair agreement with the N_H distribution of Seyfert-2s estimated by Risaliti, Maiolino & Salvati (1999). These authors find that about 75 per cent of their sample has $N_H > 10^{23} \text{ cm}^{-2}$ and at least 25 per cent has $N_H > 10^{25} \text{ cm}^{-2}$. This set of models are consistent with the unified scheme with the ratio \mathcal{R} related to the opening angle of the torus. Similar models but with a smooth transition between obscured and unobscured sources are presented by Treister et al. (2004). In this paper we use models with $\mathcal{R} = 1, 2, 3$ and 4 . We note that $\mathcal{R} = 4$ is the locally estimated value for the fraction of obscured AGN (Maiolino & Rieke 1995).

7 RESULTS

In this section we compare the observed redshift and column density distributions of the GWS sample against the predictions of the models above. To minimise incompleteness uncertainties due to either optically unidentified sources or systems without redshift determination (spectroscopic or photometric) we perform the comparison for the hard-band X-ray sources. The 2-10 keV sample has indeed, sufficient number of sources to avoid poor statistics while, about 37 per cent of them (36 out of 97) are either blank fields or do not have a redshift estimate. Selection at the 2-10 keV band also provides samples that are less sensitive to obscuration and is therefore best suited for studies on the intrinsic fraction of obscured AGN. Finally, many groups have published results for the 2-10 keV spectral band and therefore, choosing this energy range for the analysis facilitates comparison of our survey with previous samples. For the comparison with the models above, the AGN XLF is integrated in the redshift interval $z = 0 - 5$ for unobscured luminosities in the range $L_X(2 - 10 \text{ keV}) = 10^{42} - 10^{46} \text{ erg s}^{-1}$. For each luminosity and redshift interval the distribution of AGNs to different columns is described by the $f(N_H)$ models discussed in the previous section. The predicted number density of objects in each L_X , N_H and z bins are then folded through the sensitivity map of the EGS to estimate the number of AGNs to the flux limit of the survey.

7.1 The redshift distribution

Figure 6 shows the redshift distribution of the hard-band sample. For sources without spectroscopic redshifts we use the photometric redshift probability density distribution, instead of the primary solution only, to construct the histogram in Figure 6. This approach guarantees that some of the uncertainties involved in the determination of photometric redshifts are factored into our analysis. For sources assigned photometric redshifts based on the Lyman break galaxy selection (Steidel et al. 2003, 2004) we assume a Gaussian

probability density distribution with a mean and a standard deviation appropriate for the selection criteria that each source fulfills (see section 4).

A total of 36 hard X-ray selected sources (37 per cent of the sample) do not have spectroscopic or photometric redshift determination. These are shown with the hatched histogram in Figure 6. Their optical magnitude distribution is presented in the two upper panels of Figure 5. Fourteen of these 36 sources are blank fields and are most likely associated with $z > 1$ systems. The remaining 22 sources have a distribution that is skewed to fainter magnitudes in Figure 5 compared to spectroscopically identified systems but similar to that of X-ray sources with photometric redshift determination. However, 17 of these 22 sources have $B - I < 1.5$ mag and are likely to be associated with high- z QSOs. Nevertheless, unless all spectroscopically unidentified sources are clustered in a narrow redshift slice, we do not expect them to drastically modify the position of the peak of the distribution in Figure 6.

Also shown in Figure 6 are the predictions of the two model XLFs presented in the previous section for the Ueda et al. (2003) $f(N_H)$. The adopted N_H distribution has only minor effects on the resulting redshift distribution and does not affect any of our conclusions. In Figure 6 the Miyaji et al. (2000) prediction peaks at $z \approx 1.5$, higher than the observations. On the contrary, the Ueda et al. (2003) XLF produces a redshift distribution with a peak and overall shape in broad agreement with the data. There is however, a larger fraction of $z \approx 1$ sources compared to the model prediction, suggesting a cosmic variance spike. This is more clearly demonstrated in the inset plot of Figure 6 which uses a narrower logarithmic redshift bin of 0.05. The full EGS sample will have a sufficiently wide FOV (0.5 deg^2) to address this issue. The Ueda et al. luminosity function also predicts a larger number of high- z systems compared to the observations. It is possible that some of the X-ray sources without redshift determination will populate this high- z tail. We attempt to quantify the agreement between the observed and model distributions in Figure 6, in the optimal case that the spectroscopically unidentified sources are distributed to redshift bins in such a way that the difference between the observed and model $N(z)$ is minimal. In the case of the Ueda et al. (2003) XLF we estimate a χ^2 -test probability that the two distributions (model and observations) are drawn from the same parent population of about 99 per cent. For the Miyaji et al. (2000) model this exercise gives a probability of < 1 per cent.

7.2 The column density distribution

Figure 7 presents the N_H distribution of the hard X-ray selected sample. The fraction of obscured AGN ($N_H > 10^{22} \text{ cm}^{-2}$) in this figure is estimated 48 ± 9 per cent. For sources without spectroscopic or photometric redshift estimates we assume $z = 1.5$ to estimate the intrinsic N_H . Adopting a different mean z in the range $1 - 2$ for these systems however, does not significantly modify the derived N_H distribution. Also, the photometric redshift uncertainties have little impact on the observed distribution in Figure 7. Assuming a redshift dependence of the rest-frame column density of the form $N_H \propto (1 + z)^{2.65}$ (e.g. Barger et al. 2003) and a photo- z rms scatter $\delta z / (1 + z) = 0.08$ (see section 4), we estimate $\delta \log N_H = 0.09$, which is much smaller than the small photon statistics uncertainty.

Also, this plot is constructed using the N_H probability density distribution for each source instead of the best-fit solution. The advantage of this approach is that the column density uncertainties, due to small number of photons in the X-ray spectra, are taken

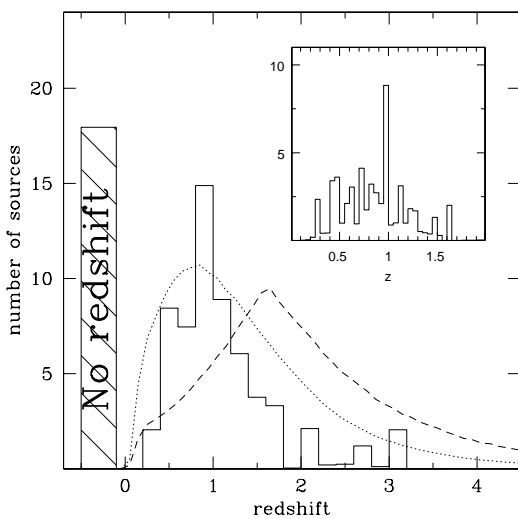


Figure 6. Redshift distribution of the hard X-ray selected sample. The hatched region shows the number of sources without spectroscopic identification. The dotted and dashed lines are the predictions of the Ueda et al. (2003) and Miyaji et al. (2000) XLFs respectively. The inset plot shows the same redshift distribution only for sources in the range $0 < z < 2$ using a narrower bin size to search for cosmic structures within the surveyed area.

into account in the analysis. Indeed, the C-statistic, used in the few counts limit, provides confidence limits and probability density distributions for the fitted parameters. In particular the ΔC is distributed as χ^2 with ν degrees of freedom (where ν is the number of fitted parameters) and hence, the same methods used to estimate confidence intervals for the model parameters in the case of the χ^2 analysis also apply to the C-statistic for spectra with few counts (Cash 1979). We confirm this by performing simulations of power-law spectra with fixed $\Gamma = 1.8$ and different levels of X-ray obscuration. We verify that even to the limit of less than ≈ 10 photons the N_H probability density distribution estimated from the C-statistic is in agreement with that derived from the simulations.

Figure 7 presents the predictions of the different $f(N_H)$ models discussed in the previous section combined with the Ueda et al. (2003) XLF. Comparison with the data suggests that the $\mathcal{R} = 2$ model is in broad agreement with the observations. The χ^2 -test probability that the two distributions are drawn from the same parent population is about 51 per cent. Higher or lower values of \mathcal{R} provide poorer fits and fail to predict the observed distribution. Using the χ^2 statistical test we estimate probabilities of 12 per cent for the $\mathcal{R} = 3$ model and < 1 per cent for the $\mathcal{R} = 1$ and 4 models. For the Ueda et al. (2003) luminosity dependent $f(N_H)$ we estimate a χ^2 -test probability of about 71 per cent, somewhat better than the $\mathcal{R} = 2$ model, the best of the step function N_H distributions with fixed ratio \mathcal{R} . We note that the adopted XLF has little effect on the model N_H distributions shown in Figure 7 and therefore, does not alter our main conclusions.

We note however, that our sample may comprise a number of Compton thick AGN ($N_H > 10^{24} \text{ cm}^{-2}$) where the direct X-ray emission is completely blocked from view and the spectrum in the *Chandra* energy band is a pure reflection continuum. Fitting a single absorbed power-law to these sources is clearly not appropriate and will produce erroneous N_H estimates. We attempt to quantify this effect by simulating reflection dominated spectra and

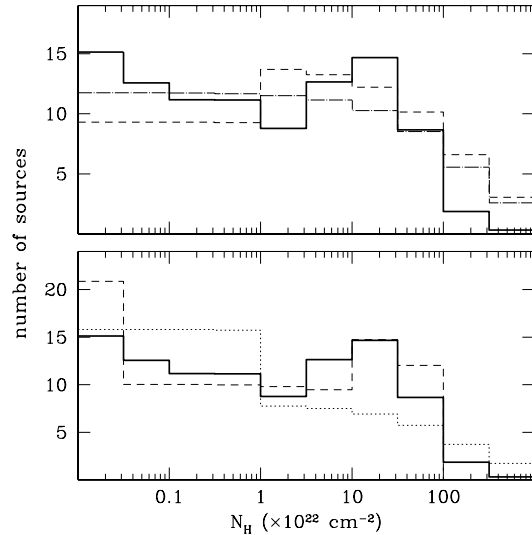


Figure 7. N_H distribution of the hard X-ray selected sample. In both panels the bold continuous line is the observed distribution. For clarity the comparison with the model predictions is split into two panels. **Upper panel:** comparison of the observations with the $\mathcal{R}=2, 3$, and 4 models described in the text corresponding to the dash-dotted, dashed and dotted lines respectively. **Lower panel:** comparison of the observations with the $\mathcal{R}=1$ model (dotted line) and the luminosity dependent N_H distribution derived by Ueda et al. (2003; dashed line). All models are for the Ueda et al. (2003) XLF.

then fitting them with `WABS*POW` XSPEC models as described in section 5. For this exercise we use the Compton reflection models of Magdziarz & Zdziarski (1995) as implemented in the PEXRAV spectral energy distribution of XSPEC. We assume a solid angle of 2π , solar abundance for all elements and an average inclination relative to the line of sight $\cos i = 0.45$. Only the reflection component was used, i.e. no direct radiation. We also add a FeKa iron line assuming a Gaussian profile with width $\sigma = 100 \text{ eV}$, similar to the instrumental FWHM of the ACIS-I and rest frame equivalent width of 1 keV appropriate for heavily obscured AGNs ($N_H > 10^{24} \text{ cm}^{-2}$; e.g. George & Fabian 1991). For the simulations we adopt a redshift $z = 1.5$ and fix the normalisation so that the spectrum has a flux of about $5 \times 10^{-15} \text{ erg s}^{-1} \text{ cm}^{-2}$ in the 2-10 keV band. The simulated spectra are fit with an absorbed power-law as described in section 5 to estimate the N_H our X-ray spectral analysis produces for this type of sources. The simulations give a narrow distribution for the estimated N_H in the range $10^{23} - 10^{24} \text{ cm}^{-2}$. We therefore underestimate the column density of these systems and it is likely that some of the sources in the range $N_H \approx 10^{23} - 10^{24} \text{ cm}^{-2}$ in Figure 7 should be moved to higher N_H values. We note however, that even if some of the sources in this column density range are reflection dominated Compton thick AGN, we do not expect this to modify our conclusions about the agreement between the data and different model N_H distributions. Unfortunately, the small number of counts in most of the obscured sources in our sample does not allow us to identify Compton thick AGN candidates dominated by reflection emission.

8 DISCUSSION

In this paper we explore the redshift and the intrinsic N_H distributions of AGN using a deep 200 ks *Chandra* pointing in the

Groth-Westphal Strip region. This is the first of a total of 8 observations that are currently underway as part of a deep wide angle (0.5 deg^2) X-ray survey in the Extended Groth Strip. A wealth of optical photometric and spectroscopic data are available in this field (e.g. DEEP2, CFHTLS) providing optical identifications as well as spectroscopic and photometric redshift estimates for the X-ray population.

The advantage of this dataset is that the detected sources are responsible for a sizable fraction of the XRB (about 70 per cent in the 2-10 keV band) and have mean X-ray spectral properties consistent with the X-ray background ($\Gamma \approx 1.4$; Nandra et al. 2005). Nevertheless they are, on average, brighter than the extremely faint X-ray population identified in the ultra-deep *Chandra* surveys (Alexander et al. 2003) facilitating follow-up multi-wavelength studies. For example, the hard X-ray selected sample comprises 97 sources of which 74 have $R < 24.5$ mag (76 per cent) and therefore are accessible for optical spectroscopy using 10-m class telescopes. For comparison, in the CDF-N a total of 332 sources are detected in the 2-8 keV spectral band of which 203 (60 per cent) have $R < 24.5$ mag and 162 (50 per cent) have optical spectroscopy available (Barger et al. 2003).

For comparison with the models we focus on the hard X-ray selected sample. This combines sufficient number of sources (97) for statistical reliability and high optical identification rate minimising uncertainties due to optically faint X-ray sources. A total of 14 systems in this sample (14 per cent) are blank fields. Many of them also have $\log f_X / f_{opt} \gtrsim 1$. This is shown in Figure 8 which plots R_{AB} -band magnitude against 2-10 keV X-ray flux. High X-ray-to-optical flux ratio systems are suggested to comprise a large fraction of high- z heavily obscured type-II QSOs (Mignoli et al. 2004; Civano, Comastri & Brusa 2005). Figure 9 plots the N_H distribution of these sources assuming a mean redshift $z = 1.5$. The optically unidentified sources in the hard sample are skewed toward high column densities compared with identified sources, with a median of about $5 \times 10^{22} \text{ cm}^{-2}$.

The redshift distribution of the GWS hard-band sample, using both spectroscopic and photometric redshifts, shows a peak at $z \approx 1$. Although about 2/5 of the X-ray sources do not have redshift determination, we argue that these systems are unlikely to modify the shape of the $N(z)$. The observed redshift distribution in Figure 6 is in agreement with previous deep surveys in the hard-band that also find that the X-ray population peaks at $z \approx 1$ (Fiore et al. 2003; Georgantopoulos et al. 2004; Barger et al. 2005; Treister et al. 2005). This is at odds with the recent versions of the population synthesis models that successfully reproduce the spectral properties of the XRB but predict a peak at higher redshifts $z \approx 1.5$ (Comastri et al. 1995; Gilli et al. 2001). As demonstrated in Figure 6, the origin of this discrepancy is that the models above adopt the XLF derived for soft-band selected powerful QSO that peak at $z \approx 1.5 - 2$ (e.g Miyaji et al. 2000). More recent studies however, that combine X-ray selected AGN samples over a wider luminosity range, suggest a more complex evolutionary history that strongly depends on L_X : more powerful systems evolve up to $z \approx 2$ while less luminous sources peak at lower redshift, $z \approx 1$ (Ueda et al. 2003; Barger et al. 2005; Hasinger, Miyaji & Schmidt 2005). As shown in Figure 6, such a luminosity dependent density evolution can successfully reproduce the redshift distribution of our sample.

The above complex evolutionary pattern warrants some physical interpretation. It is possible that less luminous systems, suggested to comprise a higher fraction of type-II AGN (Ueda et al. 2003; Barger et al. 2005; Akylas, Georgantopoulos & Georgakakis 2006), are linked to starburst activity with a peak at $z \approx 1$, while

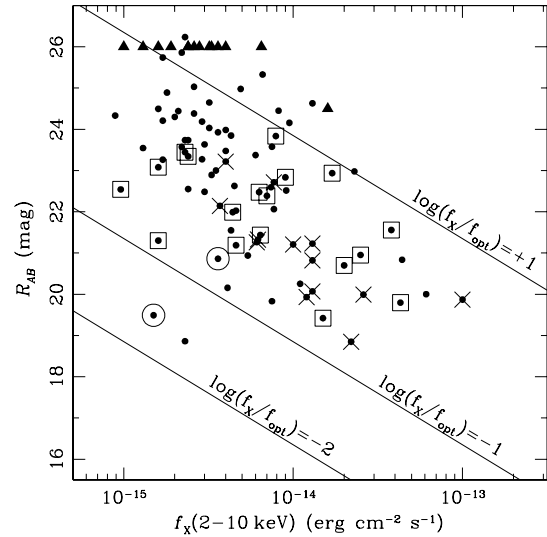


Figure 8. R_{AB} -band magnitude against 2-10 keV flux for the hard-band selected sample. The lines $\log f_X / f_{opt} = \pm 1$ delineate the region of the parameter space occupied by powerful unobscured AGNs and are estimated from the relation $\log f_X / f_{opt} = \log f_X (2 - 10 \text{ keV}) + 0.4 R_{AB} + 5.46$. A cross on top of a symbol is for sources with broad-line optical spectra. Open squares and open circles on top of a dot correspond to sources with narrow emission-line and absorption optical spectra respectively. Triangles represent upper limits in optical magnitude for sources without optical identifications.

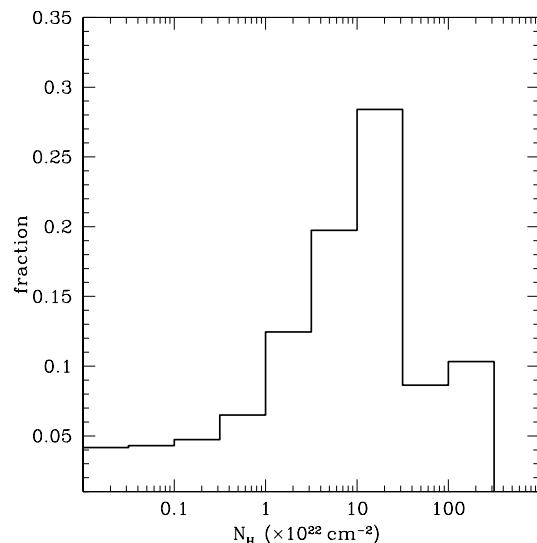


Figure 9. N_H distribution of the hard X-ray selected sources with no optical identification.

more powerful sources follow the QSO evolution peaking at $z \approx 2$. In this direction, the large fraction of hard (5-10 keV) X-ray selected sources with mid-infrared counterparts (Fadda et al. 2002) has motivated models where obscured X-ray sources are tied to the infrared-luminous population with an evolution that steeply rises to $z \approx 1$ and levels off at higher- z (Franceschini, Braito & Fadda 2002; Gandhi & Fabian 2003). These models produce a redshift distribution for the faint X-ray population with a peak at $z \approx 1$ and

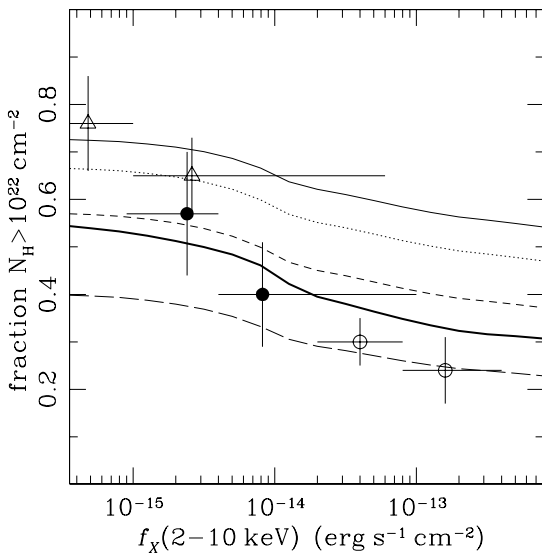


Figure 10. fraction of sources with $N_H > 10^{22} \text{ cm}^{-2}$ as a function of 2-10 keV flux. Open triangles: Chandra Deep Field South adapted from Akylas et al. (2006); Open circles: the *XMM-Newton* survey described by Akylas et al. (2006); Filled circles: this study. The thin-line curves from bottom to top correspond to models with $\mathcal{R} = 1 - 4$. The bold curve is the model that uses the Ueda et al. (2003) N_H distribution.

also provide acceptable fits to both the spectral shape of the XRB and the source counts. We note that a possible association of X-ray obscuration and star-formation activity has also been proposed to interpret the sub-mJy radio properties of X-ray selected AGNs (Bauer et al. 2002; Georgakakis et al. 2004). The models above however, require revision of the basic assumption of the unification model that requires that type-I and II sources evolve in lockstep, since they are drawn from the same parent population.

A key issue in the study of the origin of the XRB is the intrinsic N_H distribution of AGN. Even moderate amounts of gas ($N_H \approx 10^{22} \text{ cm}^{-2}$) have a strong effect on the X-ray emission below about 2 keV and therefore this issue is better addressed by observations at harder energies. In this respect, X-ray surveys in the 2-10 keV band at relatively bright fluxes ($\gtrsim 10^{-14} \text{ erg s}^{-1} \text{ cm}^{-2}$) suggest that the observed fraction of AGN with $N_H > 10^{22} \text{ cm}^{-2}$ is inconsistent with the locally determined fraction of 4:1 (Maiolino & Reike 1995) and closer to a ratio of about 1:1 (Fiore et al. 2003; Perola et al. 2004; Georgantopoulos et al. 2004; Akylas et al. 2006). Therefore, XRB models that adopt a fixed 4:1 fraction of obscured AGNs independent of redshift or luminosity have a problem reproducing the observations at bright fluxes (e.g. Treister & Urry 2005; La Franca et al. 2005; Akylas et al. 2006). Surprisingly, deeper X-ray surveys show a different picture, suggesting an abrupt increase of the fraction of obscured AGNs at faint fluxes ($\lesssim 10^{-15} \text{ erg s}^{-1} \text{ cm}^{-2}$; Perola et al. 2004; Treister et al. 2005; Akylas et al. 2006). This is demonstrated in Figure 10 plotting X-ray flux against fraction of AGN with $N_H > 10^{22} \text{ cm}^{-2}$ for both the bright *XMM-Newton* survey of Akylas et al. (2006) and the CDF-South. We note that for the latter field the N_H of each source is estimated using spectral fitting instead of hardness ratio. A full description of the spectral analysis in the CDF-South is presented by Akylas et al. (2006). In the same figure, the results from the EGS survey, split into two independent flux bins, are in broad agreement with the Akylas et al. (2006) study within the

uncertainties. Also plotted in this figure are the predictions of the different $f(N_H)$ models described in section 6 adopting the Ueda et al. (2003) XLF. We note that the adopted XLF has little effect on the model curves plotted in Figure 10. At bright fluxes the observations are in better agreement with $\mathcal{R} \approx 1$, while at fainter fluxes the data are progressively more consistent with higher \mathcal{R} models. This may suggest a luminosity dependent N_H distribution similar to that proposed by Ueda et al. (2003). This model is indeed in fair agreement with our data at intermediate fluxes but is not as successful at both the faint and the bright end of Figure 10, although somewhat better than a simple fixed- \mathcal{R} N_H distribution. This may suggest a steeper luminosity dependence of the obscured AGN fraction compared to the Ueda et al. (2003) parametrisation: i.e. ≈ 0.8 at $L_X \approx 10^{42} \text{ erg s}^{-1}$ decreasing to about 0.2 at $L_X \approx 10^{45} \text{ erg s}^{-1}$ compared to ≈ 0.6 and 0.3 respectively for the Ueda et al. (2003) model. We note that a number of recent studies, using ultra-deep and/or shallow wide-angle samples, also argue in favor of a luminosity and/or redshift dependent N_H distribution to explain the observed properties of the X-ray population (Treister & Urry 2005; La Franca et al. 2005; Akylas et al. 2006).

A luminosity dependent fraction of obscured AGN can be understood in terms of modified unification schemes. In these models the inner radius and/or the geometric height of the torus vary with the power of the central engine because of dust evaporation and radiation pressure (e.g. Lawrence 1991; Simpson 2005).

9 CONCLUDING REMARKS

This paper presents first results from an ongoing deep (200 ks per pointing) X-ray *Chandra* survey in the Extended Groth Strip region. Data from the first of a total of 8 pointings in this field are used here. We analyse and discuss the optical and X-ray properties of the sample in the context of XRB population synthesis models.

We first construct the photometric and spectroscopic redshift distribution of the 2-10 keV selected sample to the limit $\approx 8 \times 10^{-15} \text{ erg s}^{-1} \text{ cm}^{-2}$ which has a peak at $z \approx 1$ in agreement with previous studies. Although there is about 40 per cent redshift incompleteness we find that luminosity dependent density evolution, where lower luminosity systems peak at lower redshifts, is in fair agreement with the observations. Luminosity functions that assume evolution out to $z \approx 2$ for the entire AGN population (both type-I and II), similar to that of unobscured broad-line QSOs do not fit the data. The luminosity dependent evolution supported by our data is consistent with scenarios suggesting that lower-luminosity systems (dominated by obscured AGNs) are associated with star-formation activity and peak at $z \approx 1$ while, more powerful QSOs evolve out to higher- z .

We also explore the N_H distribution of the sample which is consistent with either a fixed obscured AGN fraction of $\mathcal{R} \approx 2$ or the luminosity dependent N_H distribution proposed by Ueda et al. (2003), where less luminous systems comprise a higher fraction of type-II AGNs. We also argue that such luminosity dependent parametrisation of the N_H distribution is essential to account for the fraction of obscured AGN observed in different samples over a wide range of flux limits.

The X-ray survey of the Extended Groth Strip region, when completed, will cover a total of about 0.5 deg^2 at flux limits similar to those presented here. The final sample will be about 8 times larger, comprising a total of over 1000 sources. The wealth of follow-up optical photometric and spectroscopic data available in this field (DEEP2, CFHTLS) will provide optical identifications as

well as spectroscopic and photometric redshift estimates for a large fraction of the X-ray population, for example close to 90 per cent for the hard-band. The use of *Spitzer* mid-infrared data will further increase the number of X-ray identifications and also has the potential to refine the photometric redshift estimates, particularly for the optically faint subsample. Such a high identification rate combined with photometric/spectroscopic redshifts and the complementary multi-wavelength data (infrared, radio, sub-mm) available for the EGS promise a major step forward in our understanding of the nature and the evolution of the AGN populations that make up the XRB.

10 ACKNOWLEDGMENTS

We thank the anonymous referee for valuable comments and suggestions. AG acknowledges funding from PPARC and the Marie-Curie Fellowship grant MEIF-CT-2005-025108. This work uses data obtained with support of the National Science Foundation grants AST 95-29028 and AST 00-71198. Funding for the DEEP2 survey has been provided by NSF grant AST-0071048 and AST-0071198. Some of the data presented herein were obtained at the W.M. Keck Observatory, which is operated as a scientific partnership among the California Institute of Technology, the University of California and the National Aeronautics and Space Administration. The Observatory was made possible by the generous financial support of the W.M. Keck Foundation. The DEEP2 team and Keck Observatory acknowledge the very significant cultural role and reverence that the summit of Mauna Kea has always had within the indigenous Hawaiian community and appreciate the opportunity to conduct observations from this mountain.

Based on observations obtained with MegaPrime/MegaCam, a joint project of CFHT and CEA/DAPNIA, at the Canada-France-Hawaii Telescope (CFHT) which is operated by the National Research Council (NRC) of Canada, the Institut National des Sciences de l'Univers of the Centre National de la Recherche Scientifique (CNRS) of France, and the University of Hawaii. This work is based in part on data products produced at the Canadian Astronomy Data Centre as part of the Canada-France-Hawaii Telescope Legacy Survey, a collaborative project of NRC and CNRS.

REFERENCES

Akylas A., Georgantopoulos I. & Georgakakis A., 2006, A&A, submitted
 Alexander D. M. et al., 2003, AJ, 126, 539
 Alexander D. M., Brandt W. N., Hornschemeier A. E., Garmire G. P., Schneider D. P., Bauer F. E., Griffiths R. E., 2001, AJ, 122, 2156
 Antonucci R., 1993, ARA&A, 31 473
 Babbedge T. S. R., 2004, MNRAS, 353, 654
 Baldi A., Molendi S., Comastri A., Fiore F., Matt G., Vignali C., 2002, ApJ, 564, 190B
 Barger A. J., Cowie L. L., Mushotzky R. F., Yang Y., Wang W.-H., Steffen A. T., Capak P., 2005, AJ, 129, 57
 Barger, A. J. et al. 2003, AJ, 126, 632
 Bauer F. E., Alexander D. M., Brandt W. N., Hornschemeier A. E., Vignali C., Garmire G. P., Schneider D. P., 2002, AJ, 124, 2351
 Brandt W. N. et al., 2001, AJ, 122, 2810
 Brinchmann J., et al., 1998, ApJ, 499, 112
 Bruzual A. G., Charlot S., 1993, ApJ, 405, 538
 Cash W., 1979, ApJ, 228, 939
 Civano F., Comastri A. & Brusa M., 2005, MNRAS, in press, astro-ph/0501397
 Comastri A., Setti G., Zamorani G., Hasinger G., 1995, A&A, 296, 1
 Coil A. L., Newman J. A., Kaiser N., Davis M., Ma C.-P., Kocevski D. D., Koo D. C., 2004, ApJ, 617, 765
 Coleman G. D., Wu C.-C., Weedman D. W., 1980, ApJ, 43, 393
 Downes A. J. B., Peacock J. A., Savage A., Carrie D. R., 1986, MNRAS, 218, 31
 Faber S. M., et al. 2005, ApJ, submitted, astro-ph/0506044
 Fadda D., Flores H., Hasinger G., Franceschini A., Altieri B., Cesarsky C. J., Elbaz D., Ferrando P., 2002, A&A, 383, 838
 Fiore F., et al., 2003, A&A, 409, 79
 Fomalont E. B., Windhorst R. A., Kristian J. A., Kellerman K. I., 1991, AJ, 102, 1258
 Franceschini A., Braito V., Fadda D., 2002, MNRAS, 335L, 51
 Gambill J. K., Sambruna R. M., Chartas G., Cheung C. C., Maraschi L., Tavecchio F., Urry C. M., Pesce J. E., 2003, A&A, 401, 505
 Gandhi P., Crawford C. S., Fabian A. C., Johnstone R. M., 2004, MNRAS, 348, 529
 Gandhi P. & Fabian A. C., 2003, MNRAS, 339, 1095
 Georgakakis A., Hopkins A. M., Afonso J., Sullivan M., Mobasher B., Cram L. E., 2004, MNRAS, 354, 127
 Georgakakis A., Georgantopoulos I. & Akylas A., 2006, MNRAS, 366, 171
 Georgantopoulos I., Georgakakis A., Akylas A., Stewart G. C., Giannakis O., Shanks T., Kitsionas S., 2004, MNRAS, 352, 91
 George I. M., Fabian A. C., 1991, MNRAS, 249, 352
 Giacconi R., et al., 2002, ApJS, 139, 369
 Gilli R., Salvati M., Hasinger G., 2001, A&A, 366, 407
 Groth E. J., Kristian J. A., Lynds R., O'Neil E. J. Jr., Balsano Rick, Rhodes J., 1994, AAS, 185, 5309
 Gwyn S. D. J., 2001, PhD Thesis, University of Victoria
 Gruber D. E., Matteson J. L., Peterson L. E., Jung G. V., 1999, ApJ, 520, 124
 Hasinger G., Miyaji T., Schmidt M., 2005, A&A, in press, astro-ph/0506118
 Hasinger G., 2003, Proceedings of the conference: "The restless high energy universe", Amsterdam, to be published in Nucl. Physics B. Suppl. Ser., editors E.P.J. van den Heuvel, J.J.M. in 't Zand, and R.A.M.J. Wijsers, astro-ph/0310804
 Hopkins A. M., Connolly A. J., Szalay A. S., 2000, AJ, 120, 2843
 Kim D.-W., 2004, ApJS, 150 19
 Kinney A. L., Calzetti D., Bohlin R. C., McQuade K., Storchi-Bergmann T., Schmitt H. R., 1996, ApJ, 467, 38
 Kitsionas S., Hatziminaoglou S., Georgakakis A., Georgantopoulos I., 2005, A&A, 434, 475
 Lehmer B. D., et al., 2005, ApJS, 161, 21
 Lilly S. J., Le Fevre O., Crampton David, Hammer F., Tresse L., 1995, ApJ, 455, 50
 Magdziarz & Zdziarski, 1995, MNRAS, 273, 837
 Maiolino & Rieke, 1995, ApJ, 454, 95
 Mignoli M., et al., 2004, A&A, 418, 827
 Miyaji T., Hasinger G., Schmidt M., 2000, A&A, 353, 25
 Morrison R., McCammon D., 1983, ApJ, 270, 119
 Nandra K., Pounds, K. A., 1994, MNRAS, 268, 405
 Nandra K., et al., 2005, MNRAS, 356, 568
 Perola G. C., et al., 2004, A&A, 421, 491
 Reeves J. N., Turner M. J. L., 2000, MNRAS, 316, 234
 Risaliti G., Maiolino R., Salvati M., 1999, ApJ, 522, 157
 Rosati P., et al., 2002, ApJ, 566, 667
 Sarajedini V., et al., 2006, ApJ submitted
 Steidel C. C., Adelberger K. L., Shapley A. E., Pettini M., Dickinson M., Giavalisco M., 2003, ApJ, 592, 728
 Steidel C. C., Shapley A. E., Pettini M., Adelberger K. L., Erb D. K., Reddy N. A., Hunt M. P., 2004, ApJ, 604, 534
 Treister E. & Urry M. C., 2005, ApJ, 630, 115
 Treister E., et al., 2004, ApJ, 616, 123
 Ueda Y., Akiyama M., Ohta K., Miyaji T., 2003, ApJ, 598, 886
 Virani S. N., Treister E., Urry M. C., 2006, AJ, in press, astro-ph/0506551
 Vogt N. P., 2005, ApJS, 159, 41
 Webb T. M. A., Lilly S. J., Clements D. L., Eales S., Yun M., Brodwin M., Dunne L., Gear W. K., 2003, ApJ, 597, 680

Weiner B. J., et al., 2005, ApJ, 620, 595
Willmer C. N. A., et al. 2005, ApJ, submitted, astro-ph/0506041
Wisotzki L., 1998, AN, 319, 257
York D. G., et al., 2000, AJ, 120, 1579

Table 2. Chandra GWS X-ray/optical catalogue. Col.(1): Source catalogue number; Col.(2): X-ray right ascension in J2000; Col.(3): X-ray declination in J2000; Col.(4): X-ray/optical centroid offset in arcsec; Col.(5): percent probability the optical counterpart is spurious alignment; Col.(6): R_{AB} magnitude and source of optical identification 1=DEEP2, 2=Steidel et al. (2003), 3=CFHTLS; Col.(7): spectroscopic redshift and source catalogue 1=DEEP2, 2=DEEP (Weiner et al 2005), 3: CFRS (Lilly et al. 1995), 4: Steidel et al. (2003), 5: SDSS; Col.(8): optical spectroscopic classification, NL=narrow emission lines, BL=broad emission lines, AB=absorption lines, UNCL=no classification available, STAR=Galactic star; Col.(9): photometric redshift; Col.(10): N_H in units of 10^{22} cm^{-2} ; Col.(11): unobscured 0.5-10 keV X-ray luminosity in erg s^{-1} . Col.(12): Flags fshu=source detected at $< 4 \times 10^{-6}$ probability in this band, where the bands are f=full, s=soft, h=hard, u=ultrahard.

Cat No.	α_X (J2000)	δ_X (J2000)	δ_{OX} (arcsec)	P (per cent)	R_{AB} (mag)	z_{spec}	class	z_{phot}	N_H (10^{22} cm^{-2})	$L_X(0.5 - 10 \text{ keV})$ ($10^{43} \text{ erg s}^{-1}$)	Flags
(1)	(2)	(3)	(4)	(5)	(6)	(7)	(8)	(9)	(10)	(11)	(12)
c1	14 16 42.10	+52 31 42.81	1.36	0.29	20.95 ¹	0.605 ¹	NL	$0.490^{+0.04}_{-0.04}$	$0.41^{+0.45}_{-0.28}$	6.45	fshu
c2	14 16 43.50	+52 29 02.83	0.00	0.24	24.42 ³	—	—	—	< 2.40	3.47	f
c3	14 16 44.03	+52 30 10.40	0.41	0.12	22.62 ¹	—	—	—	$2.87^{+3.16}_{-2.23}$	8.82	fsh
c4	14 16 45.39	+52 29 05.60	0.36	0.03	21.20 ¹	1.630 ¹	BL	$0.070^{+0.1}_{-0.04}$	< 1.49	19.85	fsh
c5	14 16 46.99	+52 30 00.79	—	—	< 26.00	—	—	—	$4.49^{+3.85}_{-3.17}$	6.23	fs
c6	14 16 48.80	+52 25 58.04	0.73	0.08	20.84 ¹	—	—	—	< 0.84	6.77	fs
c7	14 16 49.46	+52 25 30.75	0.06	< 0.01	20.00 ¹	—	—	—	$0.17^{+0.43}_{-0.17}$	91.80	fshu
c8	14 16 51.21	+52 20 47.00	1.35	0.29	20.70 ¹	0.808 ²	BL	$0.980^{+0.17}_{-0.36}$	< 0.32	9.48	fsh
c9	14 16 52.03	+52 27 00.54	0.79	0.64	23.47 ¹	—	—	$0.770^{+0.06}_{-0.07}$	$2.72^{+4.03}_{-2.06}$	9.06	fsh
c10	14 16 53.46	+52 21 05.54	—	—	< 24.50	—	—	—	$2.50^{+1.44}_{-1.21}$	23.17	fsh
c11	14 16 53.82	+52 21 23.79	0.00	0.01	22.06 ³	—	—	$0.620^{+0.05}_{-0.06}$	$10.05^{+7.44}_{-4.17}$	2.62	fhu
c12	14 16 58.53	+52 24 12.60	—	—	< 26.00	—	—	—	$9.57^{+6.96}_{-4.99}$	7.59	fsh
c13	14 16 59.11	+52 22 41.88	—	—	< 26.00	—	—	—	$28.77^{+36.66}_{-20.29}$	5.34	f
c14	14 16 59.26	+52 34 36.04	0.00	1.23	25.03 ³	—	—	—	$40.30^{+75.73}_{-23.82}$	9.18	fh
c15	14 17 00.03	+52 23 04.41	0.97	2.09	24.38 ¹	—	—	$1.270^{+0.16}_{-0.08}$	$16.84^{+89.76}_{-11.48}$	3.58	fh
c16	14 17 00.69	+52 19 18.58	0.34	0.01	20.25 ¹	—	—	—	< 1.15	38.42	fsh
c17	14 17 04.19	+52 21 40.46	1.09	0.82	22.59 ¹	—	—	$0.750^{+0.04}_{-0.04}$	$7.49^{+2.78}_{-2.25}$	3.96	fshu
c18	14 17 04.26	+52 24 53.78	0.44	0.01	19.42 ¹	0.281 ¹	NL	$0.370^{+0.08}_{-0.08}$	$8.82^{+2.11}_{-1.77}$	1.04	fshu
c19	14 17 05.71	+52 31 46.27	0.76	0.87	23.73 ¹	—	—	$2.200^{+0.32}_{-0.32}$	$20.58^{+42.17}_{-19.10}$	6.92	fh
c20	14 17 05.75	+52 32 30.62	0.00	0.07	22.24 ³	—	—	—	< 2.02	2.65	fs
c21	14 17 08.49	+52 32 25.40	0.00	2.03	25.59 ³	—	—	$0.920^{+0.19}_{-0.18}$	< 1.01	0.32	fs
c22	14 17 08.64	+52 29 29.72	—	—	< 26.00	—	—	$1.120^{+0.13}_{-0.13}$	< 1.19	1.63	fs
c23	14 17 08.97	+52 27 09.00	0.51	0.04	20.61 ¹	0.532 ¹	AB	$0.540^{+0.03}_{-0.04}$	$3.36^{+2.59}_{-1.89}$	0.34	f
c24	14 17 10.28	+52 34 33.95	2.96	< 0.01	21.55 ²	—	—	—	$3.99^{+1.98}_{-1.56}$	1.14	fshu
c25	14 17 10.62	+52 28 28.73	0.24	0.02	22.02 ¹	—	—	—	< 0.08	0.13	fsh
c26	14 17 11.05	+52 28 37.66	—	—	< 26.00	—	—	—	$1.19^{+1.86}_{-1.19}$	2.89	fshu
c27	14 17 11.12	+52 25 41.95	1.31	0.14	19.91 ¹	0.418 ⁴	NL	—	< 0.08	0.06	fs
c28	14 17 11.64	+52 31 32.12	0.19	0.02	22.77 ¹	0.835 ¹	NL	$0.940^{+0.33}_{-0.05}$	< 0.95	0.39	fs
c29	14 17 11.88	+52 20 11.61	0.19	< 0.01	19.79 ¹	0.433 ¹	NL	$0.600^{+0.05}_{-0.06}$	< 0.04	4.76	fshu
c30	14 17 12.90	+52 22 07.53	—	—	< 26.00	—	—	—	$3.38^{+20.00}_{-3.38}$	1.20	f
c31	14 17 14.35	+52 25 32.98	—	—	< 26.00	—	—	—	$1.65^{+4.86}_{-1.65}$	1.39	fs
c32	14 17 14.94	+52 34 20.09	0.00	3.32	24.49 ³	—	—	—	$26.68^{+97.17}_{-18.28}$	4.46	fh
c33	14 17 15.07	+52 23 12.33	0.17	< 0.01	21.32 ¹	1.263 ²	BL	$1.700^{+0.34}_{-0.34}$	$0.02^{+0.63}_{-0.02}$	8.94	fshu
c34	14 17 15.21	+52 26 49.99	1.17	0.32	21.43 ¹	0.723 ¹	NL	$0.740^{+0.07}_{-0.05}$	$5.51^{+2.15}_{-1.84}$	2.23	fshu
c35	14 17 18.89	+52 27 43.74	1.06	1.17	23.47 ¹	1.211 ¹	NL	$1.120^{+0.11}_{-0.08}$	< 2.15	0.87	f
c36	14 17 19.00	+52 30 51.04	—	—	< 26.00	—	—	—	< 3.56	0.83	fs
c37	14 17 19.32	+52 27 55.54	0.36	0.19	23.72 ¹	1.208 ¹	NL	$1.130^{+0.19}_{-0.06}$	$0.53^{+3.26}_{-0.53}$	0.97	fs
c38	14 17 20.07	+52 25 00.37	0.10	0.02	24.03 ¹	—	—	$0.460^{+0.09}_{-0.04}$	$0.33^{+0.34}_{-0.33}$	0.20	fsh
c39	14 17 20.43	+52 29 11.68	0.00	0.49	25.83 ³	—	—	—	< 2.27	1.31	fs
c40	14 17 22.98	+52 31 43.50	0.12	< 0.01	21.30 ¹	0.465 ¹	NL	$0.580^{+0.05}_{-0.04}$	< 0.58	0.24	fsh
c41	14 17 23.43	+52 31 53.54	0.10	< 0.01	21.26 ¹	0.484 ¹	BL	$0.660^{+0.06}_{-0.07}$	< 0.24	1.13	fshu
c42	14 17 23.63	+52 25 55.05	0.38	0.22	23.54 ¹	—	—	—	$24.61^{+26.83}_{-15.05}$	2.08	fh
c43	14 17 24.30	+52 32 29.61	0.43	0.19	23.26 ¹	0.902 ¹	NL	$0.830^{+0.09}_{-0.04}$	< 5.84	0.39	fs
c44	14 17 24.62	+52 30 24.55	0.10	< 0.01	19.99 ¹	0.482 ¹	BL	$0.990^{+0.46}_{-0.46}$	< 0.12	3.01	fshu
c45	14 17 25.28	+52 35 12.08	—	—	< 26.00	—	—	$0.590^{+0.57}_{-0.24}$	< 0.90	0.09	f
c46	14 17 25.37	+52 35 44.19	—	—	< 26.00	—	—	—	$4.76^{+4.15}_{-2.99}$	6.53	fsh
c47	14 17 27.08	+52 29 11.97	0.09	0.01	23.63 ¹	—	—	$4.528^{+0.45}_{-0.45}$	< 0.44	5.61	fshu
c48	14 17 27.31	+52 31 31.33	0.00	0.68	25.68 ³	—	—	—	$6.71^{+15.11}_{-6.09}$	1.81	fs
c49	14 17 29.02	+52 35 53.59	0.00	2.99	24.96 ³	—	—	—	$0.05^{+0.77}_{-0.05}$	0.26	fs
c50	14 17 29.97	+52 27 47.62	0.08	0.03	25.32 ¹	—	—	$0.610^{+0.21}_{-0.07}$	$0.29^{+0.40}_{-0.29}$	1.48	fshu

Table 2 – continued

Cat No.	α_X (J2000)	δ_X (J2000)	δ_{OX} (arcsec)	P (per cent)	R_{AB} (mag)	z_{spec}	class	z_{phot}	N_H (10^{22} cm^{-2})	L_X (0.5 – 10 keV) ($10^{43} \text{ erg s}^{-1}$)	Flags
(1)	(2)	(3)	(4)	(5)	(6)	(7)	(8)	(9)	(10)	(11)	(12)
c51	14 17 30.62	+52 22 42.95	0.39	0.51	24.79 ¹	—	—	1.160 ^{+0.12} — ^{-0.08}	1.49 ^{+2.93} — ^{-1.49}	1.51	fs
c52	14 17 30.66	+52 23 02.21	—	—	<26.00	—	—	—	< 0.89	1.72	fs
c53	14 17 30.72	+52 23 05.35	0.45	< 0.01	25.72 ²	—	—	—	< 0.56	0.50	fs
c54	14 17 30.87	+52 28 18.22	0.00	0.79	25.74 ³	—	—	0.550 ^{+0.39} — ^{-0.22}	6.10 ^{+5.35} — ^{-3.15}	0.42	fh
c55	14 17 32.65	+52 32 02.97	0.12	0.01	22.83 ¹	0.986 ¹	NL	0.820 ^{+0.11} — ^{-0.03}	0.72 ^{+0.73} — ^{-0.66}	5.53	fshu
c56	14 17 33.64	+52 20 38.86	2.44	0.96	20.94 ¹	—	—	0.530 ^{+0.05} — ^{-0.06}	14.30 ^{+14.65} — ^{-6.28}	1.55	fh
c57	14 17 33.83	+52 33 49.03	0.16	< 0.01	21.18 ¹	0.550 ¹	NL	0.640 ^{+0.04} — ^{-0.07}	2.16 ^{+1.19} — ^{-0.92}	0.84	fshu
c58	14 17 34.02	+52 24 56.12	—	—	<26.00	—	—	—	101.21 ^{+255.55} — ^{-78.05}	4.46	fh
c59	14 17 34.41	+52 31 06.63	0.14	< 0.01	19.49 ¹	0.271 ¹	AB	0.290 ^{+0.07} — ^{-0.03}	0.02 ^{+0.42} — ^{-0.02}	0.05	fsh
c60	14 17 34.87	+52 28 10.45	0.08	< 0.01	20.82 ¹	1.223 ²	BL	0.460 ^{+0.14} — ^{-0.07}	< 1.06	14.08	fshu
c61	14 17 35.98	+52 30 29.55	0.10	< 0.01	19.87 ¹	0.985 ³	BL	0.130 ^{+0.12} — ^{-0.09}	< 0.04	69.66	fshu
c62	14 17 36.32	+52 30 16.70	0.14	0.07	24.62 ¹	0.969 ⁴	NL	—	3.26 ^{+6.46} — ^{-3.26}	0.53	f
c63	14 17 36.39	+52 35 44.08	0.49	0.36	23.81 ¹	—	—	0.380 ^{+0.07} — ^{-0.19}	< 0.38	0.18	fs
c64	14 17 36.89	+52 24 29.80	0.23	0.02	22.14 ¹	2.125 ⁴	BL	2.056 ^{+0.31} — ^{-0.76}	< 1.04	13.84	fshu
c65	14 17 37.38	+52 29 21.37	—	—	<26.00	—	—	—	68.09 ^{+59.75} — ^{-36.37}	10.63	fhu
c66	14 17 38.76	+52 34 13.47	0.63	0.89	24.18 ¹	—	—	—	< 1.54	1.35	fs
c67	14 17 38.88	+52 23 32.92	0.23	0.01	21.22 ¹	2.148 ¹	BL	1.691 ^{+0.12} — ^{-0.2}	< 0.69	51.50	fshu
c68	14 17 39.06	+52 28 43.78	0.43	0.65	24.92 ¹	—	—	—	< 0.01	0.79	fs
c69	14 17 39.31	+52 28 50.16	0.12	0.01	23.26 ¹	0.997 ²	UNCL	—	< 0.01	0.99	fh
c70	14 17 39.56	+52 36 19.72	0.98	0.67	22.97 ¹	—	—	—	2.27 ^{+2.66} — ^{-1.95}	5.93	fs
c71	14 17 41.44	+52 35 45.38	0.73	0.54	23.27 ¹	—	—	1.480 ^{+0.38} — ^{-0.38}	19.64 ^{+11.17} — ^{-8.75}	7.26	fsh
c72	14 17 41.90	+52 28 23.26	0.10	< 0.01	21.55 ¹	1.148 ¹	BL	0.860 ^{+0.13} — ^{-0.03}	1.16 ^{+0.56} — ^{-0.49}	38.47	fshu
c73	14 17 42.86	+52 22 35.21	—	—	<26.00	—	—	—	< 0.01	1.11	s
c74	14 17 43.28	+52 20 23.10	0.81	0.01	17.20 ¹	0.097 ⁵	AB	0.160 ^{+0.1} — ^{-0.03}	0.15 ^{+0.97} — ^{-0.15}	0.005	fs
c75	14 17 45.47	+52 29 51.17	0.03	< 0.01	22.47 ¹	0.873 ¹	NL	0.830 ^{+0.07} — ^{-0.05}	20.77 ^{+9.40} — ^{-6.66}	5.66	fshu
c76	14 17 45.70	+52 28 01.91	1.25	0.51	21.99 ¹	0.432 ²	NL	0.400 ^{+0.06} — ^{-0.08}	0.15 ^{+0.40} — ^{-0.15}	0.41	fshu
c77	14 17 45.99	+52 30 32.32	0.09	< 0.01	22.93 ¹	0.985 ¹	NL	0.770 ^{+0.05} — ^{-0.03}	3.89 ^{+3.68} — ^{-3.46}	12.28	fshu
c78	14 17 46.17	+52 25 26.65	0.32	0.10	23.47 ¹	—	—	—	13.79 ^{+84.41} — ^{-11.41}	2.08	f
c79	14 17 46.73	+52 28 58.18	0.00	0.62	27.74 ³	—	—	—	3.36 ^{+6.94} — ^{-3.36}	1.23	fs
c80	14 17 47.01	+52 25 12.07	0.75	0.39	22.54 ¹	0.749 ¹	NL	0.700 ^{+0.05} — ^{-0.03}	0.05 ^{+358.60} — ^{-0.05}	0.11	fh
c81	14 17 47.06	+52 28 16.46	—	—	<26.00	—	—	—	1.03 ^{+8.21} — ^{-1.03}	2.17	fsh
c82	14 17 47.43	+52 35 10.39	0.65	0.44	23.21 ¹	2.746 ⁴	BL	2.930 ^{+0.26} — ^{-0.26}	0.15 ^{+3.42} — ^{-0.15}	25.79	fsh
c83	14 17 49.21	+52 28 03.28	0.37	0.14	23.08 ¹	0.996 ¹	NL	0.880 ^{+0.28} — ^{-0.02}	3.63 ^{+14.10} — ^{-3.63}	0.66	fh
c84	14 17 49.23	+52 28 11.38	0.17	0.04	23.83 ¹	0.998 ²	NL	0.830 ^{+0.07} — ^{-0.06}	0.41 ^{+0.88} — ^{-0.41}	6.62	fsh
c85	14 17 49.72	+52 31 43.46	—	—	<26.00	—	—	—	3.04 ^{+4.88} — ^{-3.04}	5.57	fshu
c86	14 17 50.19	+52 36 01.15	0.00	1.68	26.22 ³	—	—	1.100 ^{+0.25} — ^{-0.18}	< 1.44	1.51	fs
c87	14 17 50.56	+52 23 39.98	—	—	<26.00	—	—	—	14.51 ^{+27.12} — ^{-12.84}	7.42	fsh
c88	14 17 50.87	+52 36 32.47	0.57	0.73	24.18 ¹	—	—	—	0.01 ^{+0.44} — ^{-0.01}	0.01	fs
c89	14 17 51.00	+52 25 34.13	0.02	< 0.01	20.86 ¹	0.431 ¹	AB	—	21.92 ^{+20.57} — ^{-10.75}	0.78	fhu
c90	14 17 51.18	+52 23 10.96	0.17	< 0.01	19.83 ¹	—	—	0.460 ^{+0.03} — ^{-0.08}	0.35 ^{+0.35} — ^{-0.24}	0.74	fshu
c91	14 17 51.78	+52 30 46.36	0.00	0.64	24.36 ³	—	—	1.250 ^{+0.12} — ^{-0.23}	2.25 ^{+2.25} — ^{-2.25}	1.12	fs
c92	14 17 52.45	+52 28 53.14	0.14	0.02	23.92 ¹	—	—	1.080 ^{+0.08} — ^{-0.08}	20.46 ^{+20.36} — ^{-16.40}	4.46	fhu
c93	14 17 52.96	+52 28 38.53	0.43	0.04	21.39 ¹	0.671 ¹	NL	0.710 ^{+0.05} — ^{-0.05}	< 2.12	0.07	f
c94	14 17 53.13	+52 20 50.02	0.00	1.72	22.67 ³	—	—	0.830 ^{+0.07} — ^{-0.05}	0.19 ^{+2.68} — ^{-0.19}	0.40	f
c95	14 17 53.72	+52 34 46.34	0.18	0.01	22.38 ¹	0.719 ¹	NL	0.800 ^{+0.08} — ^{-0.06}	25.63 ^{+22.09} — ^{-9.68}	4.85	fhu
c96	14 17 53.99	+52 30 33.94	0.17	0.06	24.33 ¹	0.998 ²	UNCL	0.830 ^{+0.12} — ^{-0.06}	4.76 ^{+4.35} — ^{-3.15}	1.09	fsh
c97	14 17 54.25	+52 31 23.37	0.16	0.06	24.20 ¹	—	—	0.810 ^{+0.06} — ^{-0.1}	< 0.26	0.86	fsh
c98	14 17 54.58	+52 34 37.95	0.53	0.29	23.44 ¹	0.948 ¹	NL	0.850 ^{+0.3} — ^{-0.04}	28.07 ^{+35.33} — ^{-14.80}	2.82	fh
c99	14 17 55.27	+52 35 32.96	0.35	0.08	22.55 ¹	3.199 ⁴	UNCL	2.930 ^{+0.26} — ^{-0.26}	1.35 ^{+8.08} — ^{-1.35}	16.94	fsh
c100	14 17 56.76	+52 24 00.07	0.24	< 0.01	25.86 ²	—	—	—	2.21 ^{+3.26} — ^{-2.21}	3.72	fsh

Table 2 – continued

Cat No.	α_X (J2000)	δ_X (J2000)	δ_{OX} (arcsec)	P (per cent)	R_{AB} (mag)	z_{spec}	class	z_{phot}	N_H (10^{22} cm^{-2})	L_X (0.5 – 10 keV) ($10^{43} \text{ erg s}^{-1}$)	Flags
(1)	(2)	(3)	(4)	(5)	(6)	(7)	(8)	(9)	(10)	(11)	(12)
c101	14 17 56.87	+52 31 24.49	0.09	0.01	23.98 ¹	–	–	0.740 ^{+0.09} _{−0.07}	0.01 ^{+0.43} _{−0.01}	1.01	fshu
c102	14 17 56.92	+52 31 18.47	0.00	0.44	25.10 ³	–	–	–	2.23 ^{+43.55} _{−2.23}	0.53	f
c103	14 17 57.12	+52 26 30.98	0.68	< 0.01	24.45 ²	–	–	–	7.74 ^{+3.00} _{−2.57}	14.69	fshu
c104	14 17 57.48	+52 31 06.92	0.00	0.19	24.89 ³	3.026 ⁴	UNCL	3.150 ^{+0.24} _{−0.24}	20.02 ^{+20.05} _{−15.41}	14.62	fshu
c105	14 17 57.51	+52 25 46.45	0.15	0.02	23.34 ¹	0.995 ¹	NL	–	1.29 ^{+1.67} _{−1.29}	1.51	fsh
c106	14 17 58.17	+52 31 33.63	0.00	1.64	23.56 ³	–	–	–	0.12 ^{+4.13} _{−0.12}	0.42	f
c107	14 17 58.20	+52 21 53.24	0.00	0.32	22.89 ³	–	–	0.940 ^{+0.16} _{−0.08}	0.65 ^{+1.79} _{−0.65}	1.80	fsh
c108	14 17 58.97	+52 31 38.89	0.20	0.02	22.71 ¹	0.644 ⁴	BL	0.765 ^{+0.07} _{−0.08}	0.29 ^{+0.38} _{−0.29}	2.17	fshu
c109	14 17 59.32	+52 24 20.30	0.22	0.07	23.78 ¹	–	–	0.320 ^{+0.09} _{−0.12}	< 0.41	0.04	fs
c110	14 18 00.08	+52 22 23.26	0.24	0.20	24.63 ¹	–	–	1.170 ^{+0.12} _{−0.13}	4.29 ^{+4.74} _{−4.29}	11.05	fshu
c111	14 18 00.41	+52 28 22.22	0.61	0.55	23.73 ¹	–	–	–	3.11 ^{+8.05} _{−3.11}	2.33	fh
c112	14 18 00.43	+52 36 10.11	0.00	1.16	26.23 ³	–	–	–	< 1.56	5.55	fsh
c113	14 18 01.15	+52 29 41.78	0.06	< 0.01	23.04 ¹	2.907 ⁴	BL	2.930 ^{+0.26} _{−0.26}	< 6.27	5.42	fs
c114	14 18 01.37	+52 31 50.77	–	–	<26.00	–	–	1.090 ^{+0.1} _{−0.09}	10.21 ^{+14.04} _{−7.13}	1.20	fh
c115	14 18 01.67	+52 28 00.66	0.02	< 0.01	24.67 ¹	–	–	–	0.88 ^{+5.02} _{−0.88}	0.74	fs
c116	14 18 02.00	+52 35 14.53	0.32	< 0.01	19.93 ¹	1.497 ¹	BL	2.879 ^{+0.29} _{−0.31}	< 2.57	111.24	fshu
c117	14 18 02.41	+52 21 32.36	0.00	0.01	18.86 ³	–	–	0.230 ^{+0.09} _{−0.05}	< 0.27	0.05	fsh
c118	14 18 02.93	+52 35 47.11	0.00	0.26	24.97 ³	–	–	–	0.59 ^{+1.42} _{−0.59}	8.09	fshu
c119	14 18 04.55	+52 36 33.15	0.43	0.28	23.57 ¹	–	–	0.810 ^{+0.29} _{−0.04}	1.01 ^{+0.61} _{−0.54}	4.81	fshu
c120	14 18 04.90	+52 27 40.14	0.18	0.07	24.30 ¹	–	–	0.780 ^{+0.05} _{−0.08}	0.15 ^{+0.68} _{−0.15}	0.79	fsh
c121	14 18 05.30	+52 25 10.63	0.80	1.42	24.44 ¹	–	–	0.770 ^{+0.31} _{−0.07}	0.77 ^{+1.23} _{−0.77}	0.82	fsh
c122	14 18 06.51	+52 33 58.67	0.84	0.72	23.19 ¹	–	–	–	1.29 ^{+4.35} _{−1.29}	1.26	fs
c123	14 18 07.07	+52 25 23.41	–	–	<26.00	–	–	0.750 ^{+0.4} _{−0.07}	1.78 ^{+1.07} _{−1.00}	2.49	fsh
c124	14 18 07.33	+52 30 30.52	0.85	0.51	22.58 ¹	0.990 ³	NL	0.850 ^{+0.08} _{−0.07}	< 13.12	0.10	s
c125	14 18 08.06	+52 27 50.36	–	–	<26.00	–	–	–	< 12.52	1.09	f
c126	14 18 08.94	+52 31 50.84	–	–	<26.00	–	–	–	339.29 ^{+271.69} _{−196.63}	34.55	f
c127	14 18 09.12	+52 28 04.04	–	–	<26.00	–	–	–	6.71 ^{+6.10} _{−3.67}	6.98	fshu
c128	14 18 11.26	+52 30 11.48	0.86	1.12	23.79 ¹	2.910 ⁴	UNCL	3.090 ^{+0.22} _{−0.22}	15.47 ^{+15.47} _{−15.47}	6.54	fs
c129	14 18 12.16	+52 28 00.29	–	–	<26.00	–	–	–	4.00 ^{+3.29} _{−3.29}	3.47	fs
c130	14 18 13.19	+52 31 13.47	–	–	<26.00	–	–	0.950 ^{+0.27} _{−0.07}	0.68 ^{+1.15} _{−0.68}	1.76	fsh
c131	14 18 13.33	+52 24 14.90	0.00	1.45	26.81 ³	–	–	1.230 ^{+0.15} _{−0.08}	1.07 ^{+3.37} _{−0.07}	1.53	fs
c132	14 18 13.96	+52 26 24.79	–	–	<26.00	–	–	–	23.97 ^{+24.61} _{−15.99}	5.17	fh
c133	14 18 14.27	+52 28 10.99	1.02	0.49	22.22 ¹	2.818 ⁴	BL	2.552 ^{+0.25} _{−0.26}	< 1.65	8.47	fs
c134	14 18 15.36	+52 32 47.61	0.00	1.29	24.28 ³	–	–	–	0.87 ^{+1.57} _{−0.87}	0.93	fs
c135	14 18 16.29	+52 29 40.30	0.18	< 0.01	20.07 ¹	1.603 ³	BL	1.700 ^{+0.34} _{−0.34}	< 0.27	34.39	fshu
c136	14 18 16.35	+52 25 24.05	0.61	0.83	24.18 ¹	–	–	–	0.58 ^{+1.45} _{−0.58}	3.47	fsh
c137	14 18 16.43	+52 33 29.77	0.12	0.03	24.22 ¹	–	–	–	< 1.53	0.29	fs
c138	14 18 16.73	+52 23 07.98	0.75	0.57	23.37 ¹	–	–	–	< 0.32	1.23	fsh
c139	14 18 18.04	+52 32 01.28	0.99	3.31	24.64 ¹	–	–	0.390 ^{+0.07} _{−0.12}	1.44 ^{+1.25} _{−0.99}	0.17	fs
c140	14 18 19.92	+52 21 15.80	–	–	<26.00	–	–	1.062 ^{+0.12} _{−0.12}	9.76 ^{+16.39} _{−7.03}	2.85	f
c141	14 18 20.30	+52 33 51.08	1.85	3.51	23.15 ¹	–	–	2.200 ^{+0.32} _{−0.32}	0.02 ^{+4.52} _{−0.02}	5.97	fs
c142	14 18 21.37	+52 26 55.46	–	–	<26.00	–	–	–	< 5.18	1.83	fs
c143	14 18 21.39	+52 32 54.31	0.44	0.29	23.57 ¹	–	–	–	3.58 ^{+4.28} _{−3.22}	0.82	fsh
c144	14 18 21.79	+52 29 55.82	0.90	0.06	19.71 ¹	0.000 ³	STAR	–	–	–	fs
c145	14 18 22.08	+52 26 50.20	0.55	0.14	22.06 ¹	–	–	0.740 ^{+0.06} _{−0.04}	0.60 ^{+1.31} _{−0.60}	0.64	fs
c146	14 18 22.41	+52 36 07.45	1.31	3.83	24.15 ¹	–	–	–	0.57 ^{+1.13} _{−0.57}	15.50	fshu
c147	14 18 22.84	+52 27 10.11	1.54	0.07	18.26 ¹	0.281 ⁵	AB	0.530 ^{+0.04} _{−0.05}	< 0.08	0.04	fs
c148	14 18 23.07	+52 21 14.50	0.00	0.73	23.84 ³	–	–	1.050 ^{+0.06} _{−0.07}	10.50 ^{+7.59} _{−6.21}	4.81	fh
c149	14 18 24.97	+52 23 30.55	0.66	0.31	22.97 ¹	–	–	1.040 ^{+0.16} _{−0.08}	3.48 ^{+2.17} _{−2.10}	17.92	fshu
c150	14 18 25.52	+52 23 49.48	0.10	< 0.01	22.51 ¹	–	–	–	0.31 ^{+0.91} _{−0.31}	2.52	fshu
c151	14 18 26.36	+52 28 18.80	0.81	0.68	23.00 ¹	–	–	–	< 0.79	7.16	fsh
c152	14 18 26.44	+52 32 35.01	0.71	0.04	19.91 ¹	–	–	0.730 ^{+0.01} _{−0.01}	< 0.27	0.33	fs
c153	14 18 26.51	+52 25 59.70	0.98	< 0.01	24.65 ²	–	–	–	12.00 ^{+10.85} _{−6.92}	5.89	fsh
c154	14 18 29.76	+52 27 09.39	0.56	0.15	22.48 ¹	–	–	0.720 ^{+0.05} _{−0.03}	6.36 ^{+4.97} _{−3.18}	1.30	fh
c155	14 18 30.24	+52 22 12.14	0.16	< 0.01	20.83 ¹	–	–	–	< 0.13	107.14	fshu
c156	14 18 32.87	+52 23 49.48	0.74	0.06	20.15 ¹	–	–	–	< 2.33	29.17	fsh
c157	14 18 37.96	+52 20 34.62	–	–	<26.00	–	–	–	< 1.52	2.53	s
c158	14 18 38.18	+52 23 58.55	1.99	0.18	18.84 ¹	1.118 ⁵	BL	1.500 ^{+0.15} _{−0.17}	< 0.21	17.79	fsh